SAPIENZA
UNIVERSITÀ DI ROMA

Dottorato di Ricerca in Statistica Metodologica

Tesi di Dottorato - XXIX Ciclo - anno 2017

Dipartimento di Scienze Statistiche

Spatial analysis of photoreceptor mosaic from Adaptive Optics images of the human retina

Thesis Supervisor:

Chiar.mo Prof.

Maurizio Vichi

Dottoranda:

Ing. Daniela Giannini

L'occhio, che si dice finestra dell'anima,
è la principale via donde il comune senso
può più copiosamente e magnificamente
considerare le infinite opere di natura.

Trattato della pittura,
Leonardo Da Vinci

A tutte le persone che lasciano
il cammino della vita
troppo presto.

Index

Chapter 1

The eye and the adaptive optics retinal imaging

Chapter 2

Reliability and agreement between metrics of cone spacing in adaptive optics images of the human retinal photoreceptor mosaic

Chapter 3

Statistical analysis of second-order properties of cone mosaic

LIST OF ABBREVIATIONS

RGC - retina ganglion cells

RNFL - retinal nerve fibre layer

ONH - optic nerve head

ONL - outer nuclear layer

INL - inner nuclear layer

GCL - ganglion cell layer

OPL - outer plexiform layer

IPL - inner plexiform layer

OS - outer segment

IS - inner segment

ATP - adenosine triphosphate

cGMP - cyclic guanosine monophosphate

LOA - low-order aberrations

HOA - high-order aberrations

WA - wavefront aberration

AO - adaptive optics

CCD - charge-coupled device

DM - deformable mirror

SLD - super luminescent diode

Scc - center-to-center spacing

LCS - local cone spacing

DRPD - density recovery profile distance

NND - nearest neighbour distance

DRP - density recovery profile

NPDR - non proliferative diabetic retinopathy

ETDRS - early treatment diabetic retinopathy study

RP - retinitis pigmentosa

PRL - preferred retinal location

RMF - retinal magnification factor

ICC - intraclass correlation coefficient

LoA - limits of agreement

OMD - occult macular dystrophy

SLO - scanning laser ophthalmoscopy

CSR - complete spatial randomness

RSA - random sequential addition

IRD - inherited retinal disease

OCT - optical coherence tomography

Chapter 1

The eye and the adaptive optics retinal imaging

1.1 The eye: how we see

The human eye functions as an optical system whose purpose is to bring the outside world into focus on the retina, thereby allowing us to see [1].

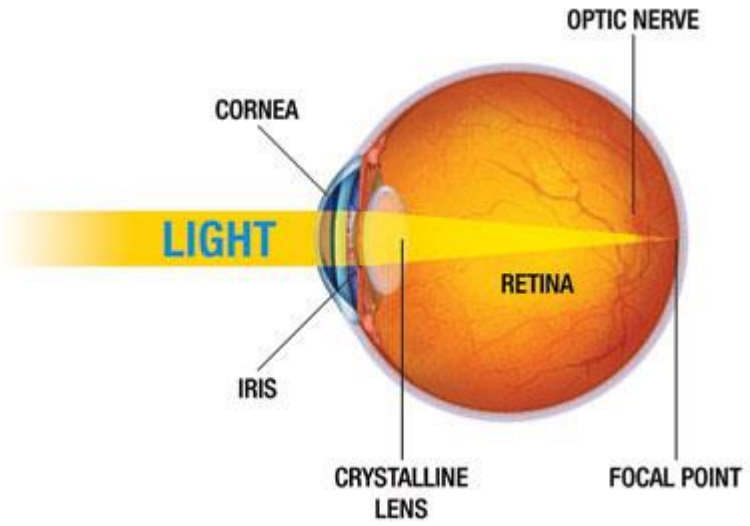

Figure 1.1 Eye image from https://www.nkcf.org/about-keratoconus/how-the-human-eye-works/.

Light rays enter the eye through the cornea (about 8 mm of diameter) and pass freely through the pupil, the opening in the center of the iris, through which light enters the eye. The iris can enlarge and shrink, like a shutter in a camera. After, the light rays pass through the eye's crystalline lens that like the lens in a camera, shortens and lengthens its width to focus light rays properly. Light rays pass through a dense, transparent gel-like substance, called the vitreous that fills the globe of the eyeball and helps the eye hold its spherical shape. Then, the light rays come to a sharp focusing point on the retina, the fovea. The retina functions like the film in a camera: captures all the light rays, and transforms this image into electrical impulses that are carried by the optic nerve to the brain (Figure 1.1).

In the retina, the light continues travelling through all the retinal layers until it reaches the photoreceptor layers. Once at the photoreceptor layers, the luminance of the light activates the rods and the cones. This produces a chemical reaction with the cones and the rods causing a propagation of neural signal that stimulates bipolar cells. The process activates the retina ganglion cells (RGCs) and the signal passes through the axons of the ganglion cells or retinal nerve fibre layer (RNFL) and optic nerve to reach the visual centre at the back of the brain via the optic nerve head (ONH). At this point, the neural signal undergoes further processing in the visual cortex of the brain before vision take place.

1.2 The retina

The retina remains the best studied part of the human brain: embryologically part of the central nervous system, but readily and noninvasively accessible to examination, it can be investigated with relative ease by both scientists and clinicians [2]. Optical examination of internal structures of the eye began as early as 1704 when Jean Méry observed feline retinal vasculature and optic disk structure [3]. Subsequent observations of the internal structures of the eye were facilitated by Charles Babbage's invention of the ophthalmoscope in 1847, and subsequent implementation by Herman Helmholtz [4]. Modern versions of his original design are principally the same and are still in use today, allowing direct observation of gross structures within the eye (Figure 1.2).

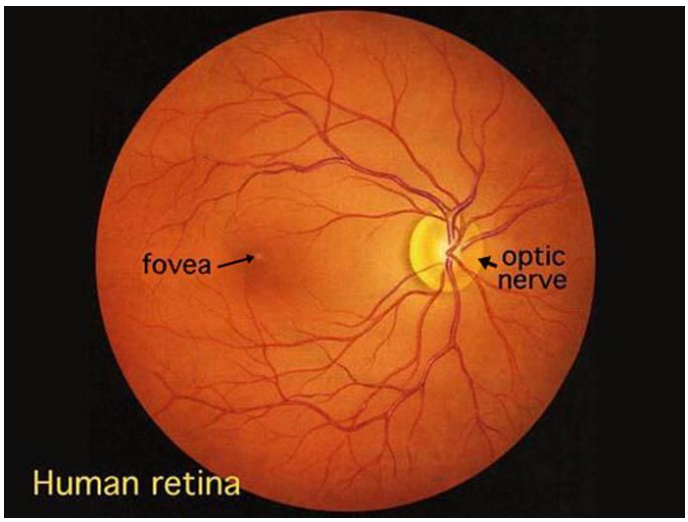

Figure 1.2 A view of the retina seen through an ophthalmoscope.

The retina has a unique cytoarchitecture with its sophisticated neurocircuitry, and is the neurosensory component of the eye. Its outer part is supplied by a vascular layer, the choroid, and protected by a tough outer layer, the sclera. The cellular elements of the retina are arranged and adapted to meet the functional requirements of the different regions of the retina. The different retinal layers are showed in Figure 1.3.

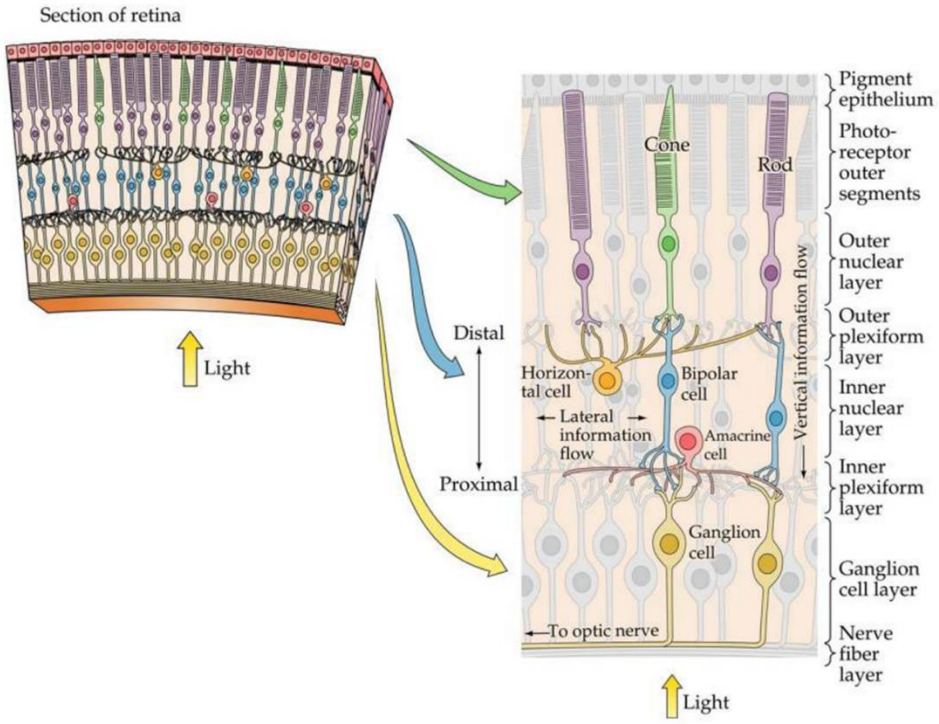

Figure 1.3 Anatomy of the different retinal layers. (Image from the web site http://www.rci.rutgers.edu/~uzwiak/AnatPhys/Vision.htm)

All vertebrate retinas are composed of three layers of nerve cell bodies and two layers of synapses. The outer nuclear layer (ONL) contains cell bodies of the rods and cones, the inner nuclear layer (INL) contains cell bodies of the bipolar, horizontal and amacrine cells and the ganglion cell layer (GCL) contains cell bodies of ganglion cells and displaced amacrine cells. Dividing these nerve cell layers are two neuropils where synaptic contacts occur. The first area of neuropil is the outer plexiform layer (OPL) where connections between rod and cones, and vertically running bipolar cells and horizontally oriented horizontal cells occur. The second neuropil of the retina, is the inner plexiform layer (IPL), and it functions as a relay station for the vertical-information-carrying nerve cells, the bipolar cells, to connect to ganglion cells. In addition, different varieties of horizontally- and vertically-directed amacrine cells, somehow interact in further networks to influence and integrate the ganglion cell signals. It is at the culmination of all this neural processing in the inner plexiform layer (IPL) that the message concerning the visual image is transmitted to the brain along the optic nerve [5].

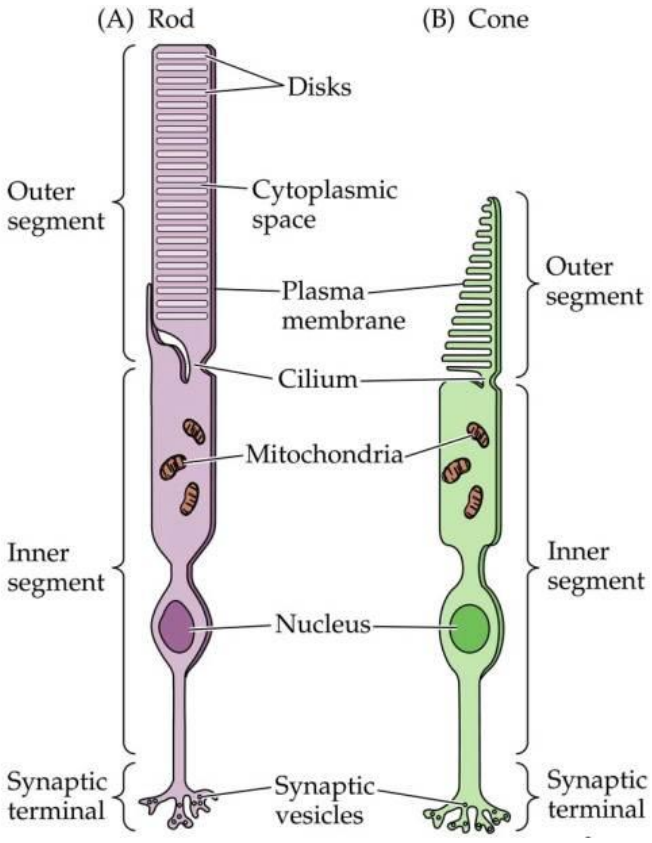

Figure 1.4 The structure of a single rod (A) and cone (B) photoreceptor from the adult human retina. The outer segment (OS) of a photoreceptor houses the machinery necessary to detect light. The inner segment (IS) is responsible for the production of energy and metabolites that will be shipped to the outer segment. The cell body is responsible for mediating cell function, and synaptic terminals are responsible for carrying the signal to the innervated bipolar cells. (Image from the web site http://www.rci.rutgers.edu/~uzwiak/AnatPhys/Vision.htm)

The photoreceptors (Figure 1.4) are the sensors of the visual system that convert the capture of photons into a nerve signal in a process called phototransduction. The human retina contains approximately four to five million cones and 77–107 million rods. Only cones are found in the foveola, whereas rods predominate outside the foveola in the remaining fovea and all of the peripheral retina. Each photoreceptor consists of an outer segment (photopigment), inner segment (mitochondria, endoplasmatic reticulum), a nucleus, an inner fiber (analogous to an axon), and the synaptic terminal. The outer segment contains the photon-capturing photopigment. Opsin is a transmembranous protein that anchors the photopigment in the plasma membrane. In the outer segments, the plasma membrane is stacked into hundreds of flat discs, thereby increasing the density of retinal-opsin photopigment per photoreceptor cell. The discs in cones are deep invaginations of the outer segment membrane, while in rods, the discs are separate from the outer segment (except at the base). Shed discs are phagocytosed by the RPE. A nonmotile cilium connects the outer and inner segments. The inner segment contains the cellular machinery necessary to meet the high metabolic requirements of the photoreceptor cells. Its outer portion (the ellipsoid) is packed with mitochondria that produce ATP by oxidative phosphorylation, while the inner portion (the myoid) contains smooth and rough endoplasmic reticulum for synthetic activity as well as microtubules for intracellular transport. The photoreceptor nucleus contains all nonmitochondrial DNA. The inner fiber is the axon of the photoreceptor cell and transmits the photoreceptor cell signals to the outer plexiform layer (OPL) via its synaptic terminals. Due to the absence of inner nuclear layer cells in the foveola, foveolar inner fibers have to travel to the OPL in the surrounding macula to make synaptic contact. The synaptic neurotransmitter of the photoreceptor cell is glutamate, which is released in response to depolarization. The terminal endings of the photoreceptors interact with neighboring photoreceptors and interneurons (horizontal and bipolar cells) and play a critical physiological role in the transmission and early processing of visual information in the retina [2].

1.3 Phototransduction

In most sensory systems, activation of a receptor by the appropriate stimulus causes the cell membrane to depolarize, ultimately stimulating an action potential and transmitter release onto the neurons it contacts. In the retina, however, photoreceptors do not exhibit action

potentials; rather, light activation causes a graded change in membrane potential and a corresponding change in the rate of transmitter release onto postsynaptic neurons. Indeed, much of the processing within the retina is mediated by graded potentials, largely because action potentials are not required to transmit information over the relatively short distances involved.

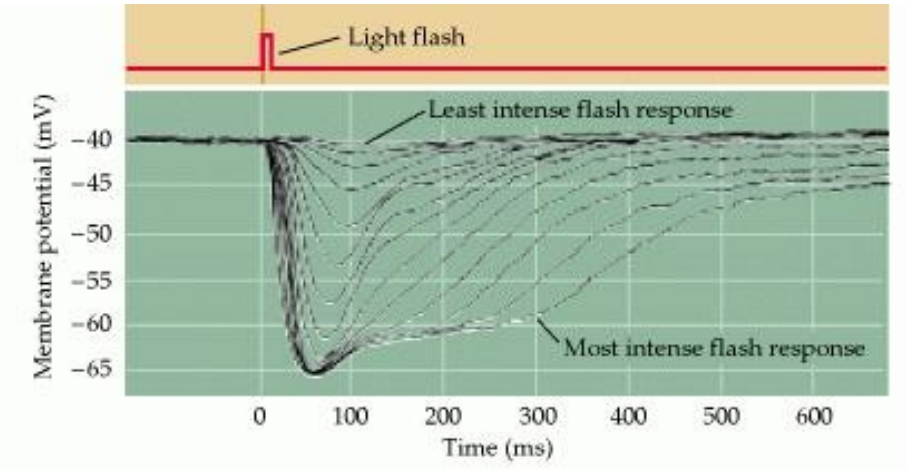

Figure 1.5 An intracellular recording from a single cone stimulated with different amounts of light (the cone has been taken from the turtle retina, which accounts for the relatively long time course of the response). Each trace represents the response to a brief flash that was varied in intensity. At the highest light levels, the response amplitude saturates (at about -65 mV). The hyperpolarizing response is characteristic of vertebrate photoreceptors; interestingly, some invertebrate photoreceptors depolarize in response to light [6].

Perhaps even more surprising is that shining light on a photoreceptor, either a rod or a cone, leads to membrane hyperpolarization rather than depolarization (Figure 1.5). In the dark, the receptor is in a depolarized state, with a membrane potential of roughly -40 mV (including those portions of the cell that release transmitters). Progressive increases in the intensity of illumination cause the potential across the receptor membrane to become more negative, a response that saturates when the membrane potential reaches about -65 mV. Although the sign of the potential change may seem odd, the only logical requirement for subsequent visual processing is a consistent relationship between luminance changes and the rate of transmitter release from the photoreceptor terminals. As in other nerve cells, transmitter release from the synaptic terminals of the photoreceptor is dependent on voltage-sensitive Ca^{2+} channels in the terminal membrane. Thus, in the dark, when photoreceptors are relatively depolarized, the number of open Ca^{2+} channels in the synaptic terminal is high, and the rate of transmitter release is correspondingly great; in the light, when receptors are hyperpolarized, the number of open Ca^{2+} channels is reduced, and the rate of transmitter

release is also reduced. The reason for this unusual arrangement compared to other sensory receptor cells is not known.

The relatively depolarized state of photoreceptors in the dark depends on the presence of ion channels in the outer segment membrane that permit Na^+ and Ca^{2+} ions to flow into the cell, thus reducing the degree of inside negativity (Figure 1.6). The probability of these channels in the outer segment being open or closed is regulated in turn by the levels of the nucleotide cyclic guanosine monophosphate (cGMP). In darkness, high levels of cGMP in the outer segment keep the channels open. In the light, however, cGMP levels drop and some of the channels close, leading to hyperpolarization of the outer segment membrane, and ultimately the reduction of transmitter release at the photoreceptor synapse.

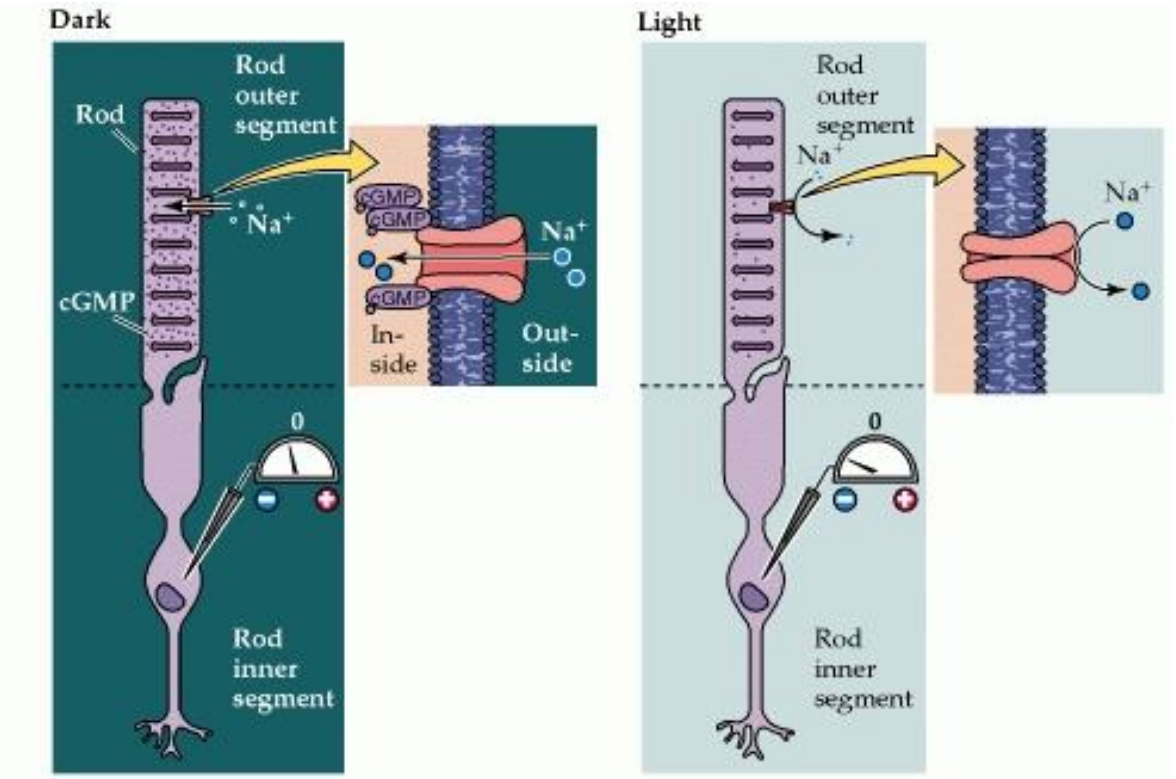

Figure 1.6. Cyclic GMP-gated channels in the outer segment membrane are responsible for the light-induced changes in the electrical activity of photoreceptors (a rod is shown here, but the same scheme applies to cones). In the dark, cGMP levels in the outer segment are high; this molecule binds to the Na+-permeable channels in the membrane, keeping them open and allowing sodium (and other cations) to enter, thus depolarizing the cell. Exposure to light leads to a decrease in cGMP levels, a closing of the channels, and receptor hyperpolarization. (Image from the web site http://www.rci.rutgers.edu/~uzwiak/AnatPhys/Vision.htm)

The series of biochemical changes that ultimately leads to a reduction in cGMP levels begins when a photon is absorbed by the photopigment in the receptor disks. The photopigment contains a light-absorbing chromophore (retinal, an aldehyde of vitamin A) coupled to one

of several possible proteins called opsins that tune the molecule's absorption of light to a particular region of the spectrum. Indeed, it is the different protein component of the photopigment in rods and cones that contributes to the functional specialization of these two receptor types. Most of what is known about the molecular events of phototransduction has been gleaned from experiments in rods, in which the photopigment is rhodopsin (Figure 1.7A); however, there is evidence that much of the inactivation process is paralleled in cones [7,8,9].

When the retinal moiety in the rhodopsin molecule absorbs a photon, its configuration changes from the 11-cis isomer to all-trans retinal; this change then triggers a series of alterations in the protein component of the molecule (Figure 1.7B). The changes lead, in turn, to the activation of an intracellular messenger called transducin, which activates a phosphodiesterase that hydrolyzes cGMP. All of these events take place within the disk membrane. The hydrolysis by phosphodiesterase at the disk membrane lowers the concentration of cGMP throughout the outer segment, and thus reduces the number of cGMP molecules that are available for binding to the channels in the surface of the outer segment membrane, leading to channel closure.

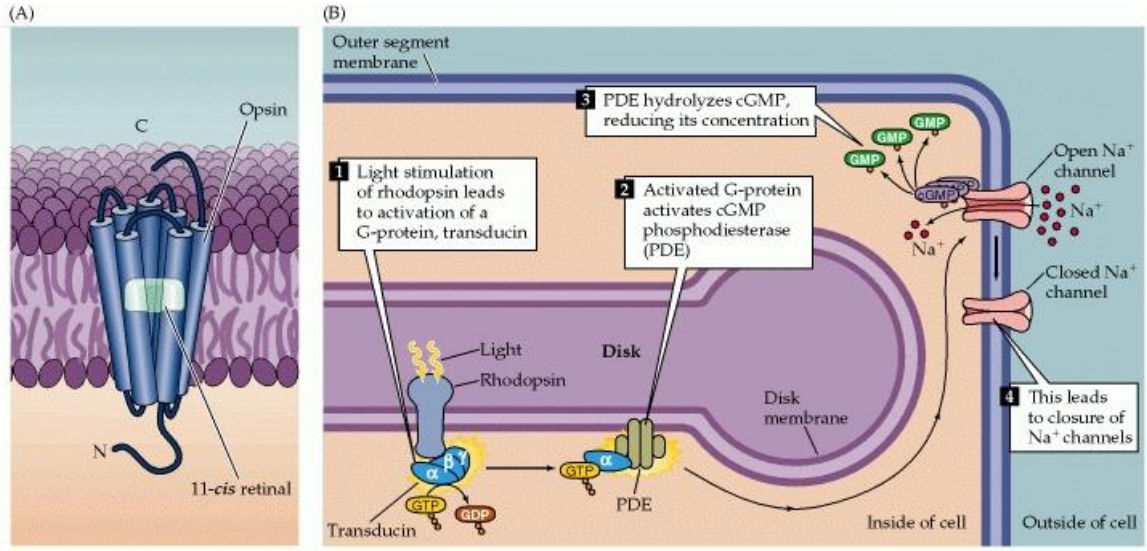

Figure 1.7. Details of phototransduction in rod photoreceptors. (A) The molecular structure of rhodopsin, the pigment in rods. (B) The second messenger cascade of phototransduction. Light stimulation of rhodopsin in the receptor disks leads to the activation of a G-protein (transducin), which in turn activates a phosphodiesterase (PDE). The phosphodiesterase hydrolyzes cGMP, reducing its concentration in the outer segment and leading to the closure of sodium channels in the outer segment membrane. (Image from the web site http://www.rci.rutgers.edu/~uzwiak/AnatPhys/Vision.htm)

One of the important features of this complex biochemical cascade initiated by photon capture is that it provides enormous signal amplification. It has been estimated that a single light-activated rhodopsin molecule can activate 800 transducin molecules, roughly eight percent of the molecules on the disk surface. Although each transducin molecule activates only one phosphodiesterase molecule, each of these is in turn capable of catalyzing the breakdown of as many as six cGMP molecules. As a result, the absorption of a single photon by a rhodopsin molecule results in the closure of approximately 200 ion channels, or about 2% of the number of channels in each rod that are open in the dark. This number of channel closures causes a net change in the membrane potential of about 1 mV.

Equally important is the fact that the magnitude of this amplification varies with the prevailing levels of illumination, a phenomenon known as light adaptation. At low levels of illumination, photoreceptors are the most sensitive to light. As levels of illumination increase, sensitivity decreases, preventing the receptors from saturating and thereby greatly extending the range of light intensities over which they operate. The concentration of Ca^{2+} in the outer segment appears to play a key role in the light-induced modulation of photoreceptor sensitivity. The cGMP-gated channels in the outer segment are permeable to both Na^{+} and Ca^{2+}; thus, light-induced closure of these channels leads to a net decrease in the internal Ca^{2+} concentration. This decrease triggers a number of changes in the phototransduction cascade, all of which tend to reduce the sensitivity of the receptor to light. For example, the decrease in Ca^{2+} increases the activity of guanylate cyclase, the cGMP synthesizing enzyme, leading to an increase in cGMP levels. Likewise, the decrease in Ca^{2+} increases the affinity of the cGMP-gated channels for cGMP, reducing the impact of the light-induced reduction of cGMP levels. The regulatory effects of Ca^{2+} on the phototransduction cascade are only one part of the mechanism that adapts retinal sensitivity to background levels of illumination; another important contribution comes from neural interactions between horizontal cells and photoreceptor terminals.

Once initiated, additional mechanisms limit the duration of this amplifying cascade and restore the various molecules to their inactivated states. The protein arrestin, for instance, blocks the ability of activated rhodopsin to activate transducin, and facilitates the breakdown of activated rhodopsin. The all-trans retinal then dissociates from the opsin, diffuses into the cytosol of the outer segment, and is transported out of the outer segment and into the pigment epithelium, where appropriate enzymes ultimately convert it to 11-cis retinal. After it is transported back into the outer segment, the 11-cis retinal recombines with opsin in the receptor disks. The recycling of rhodopsin is critically important for maintaining the light sensitivity of photoreceptors. Even under intense levels of illumination, the rate of

regeneration is sufficient to maintain a significant number of active photopigment molecules [10].

1.4 The Optical System of the Human Eye

As seen, the human eye functions as an optical system and consists of three main components: the cornea, the crystalline lens and in between them the iris. The cornea, the outermost optical element, is responsible for about 2/3 of the optical power and aberrations of the eye. The iris controls the amount of light coming into the retina by regulating the pupil diameter. The pupil has important consequences for image formation: a smaller pupil increases the depth of focus and minimizes the effects of high-order aberrations, on the contrary, the magnitude of aberrations increases with pupil dilation leading to a decrease in both visual performance and optical quality of the retinal image [1].

The crystalline lens accounts for about 1/3 of the optical power of the eye but it is capable of changing its focusing properties: controlled changes in the shape and thickness of the crystalline lens allow the eye to accommodate, the process by which the eye focuses on near objects.

Even in the normal eye, the optics and how they are aligned are not perfect, with the consequence that incoming light rays deviate from the desired path that reaches the foveal center. The deviations are defined as optical aberrations and can be classified into low-order (LOA) and high-order aberrations (HOA). LOA are the predominant optical aberrations, 90% of the overall wavefront aberration (WA) of the eye, and include defocus (hyperopia and myopia), the dominant aberration, followed by astigmatism. It is well known that HOA cannot yet be accurately corrected and greatly diminish the overall optical quality of the eye, though their contribution to the overall WA of the eye is $\leq$10% [11,12].

Aberrations impair ocular vision by bluring images formed on the retina, and decrease the quality in images taken of the retina by ophthalmic imaging cameras. To significantly improve visual performance and retinal imaging the eye's WA have to be measure and correct.

The presence of HOA, beyond defocus and astigmatism, has been known by researchers since the 19th century, but only in the 1990s wavefront sensors have been developed to allow routine estimation of the eye's WA.

Adaptive optics (AO) is a technology used to improve the performance of optical systems by minimizing aberrations. An AO ophthalmic device measures and corrects for the fluctuations of the eye's WA, with improvement of the resolution of images taken from the eye. This technology has been developed for astronomical telescopes to remove the effect of atmospheric turbulence from astrophysics objects and only in recent years has been extended to ophthalmology [13,14]. By correcting ocular aberrations, AO retinal imaging can improve the resolution to 2 μm, providing information about the retinal microstructures not allowed with current retinal imaging techniques. Retinal imaging with AO technology represents a sensitive and accurate diagnostic tool to support the ophthalmologists in the diagnosis of retinal diseases at an early stage, and in the monitoring of the effects of new therapeutic treatments at microscopic scale.

1.5 Adaptive Optics Technology for Retinal Imaging

In the late 1990s, the principles and technologies of adaptive optics (AO), originally developed for astronomy, were adapted to image the retina. The history of adaptive optics for ophthalmic imaging is just over 20 years old. Adaptive optics by itself does not provide a retinal image, rather an AO subsystem must be incorporated into an imaging device. In 1989, Dreher *et al.* used AO for the correction of second order optical aberrations of the eye [15]. Only in 1997, AO technology was successfully applied to high resolution imaging in the human eye by Liang *et al.* [16]. Since that time AO technology has been incorporated in almost all existing ophthalmic modalities to enhance quality and resolution of the retinal images: flood illumination fundus imaging, confocal scanning laser ophthalmoscopy and ophthalmic optical coherence tomography.

A typical AO retinal imaging camera has three principal components: a wavefront sensor, a corrective element and a control system, Figure 1.8. The wavefront sensor and corrector measure and correct the eye's wave aberrations respectively.

The wavefront sensor is used to measure the structure of the aberrations of the eye, with the Shack-Hartmann design being the most commonly used type. It consists of an array of lenslets, where each lenslet samples a local portion of the incident wavefront and focuses this light on a charge-coupled device (CCD). The displacement of any given spot from its intended position is directly related to the slope and amplitude of the wavefront in that portion of the pupil.

The corrective element (the “adaptive” optical element) is used to compensate for these aberrations, most commonly by using a deformable mirror, which relies on a series of actuators to deflect the mirror surface. There are many types of deformable mirrors in use in AO retinal imaging systems [14].

The AO controller, programmed with a computer, controls the interaction between the wavefront sensor and the corrector element; it interprets the wavefront sensor data and computes the appropriate wavefront corrector drive signals.

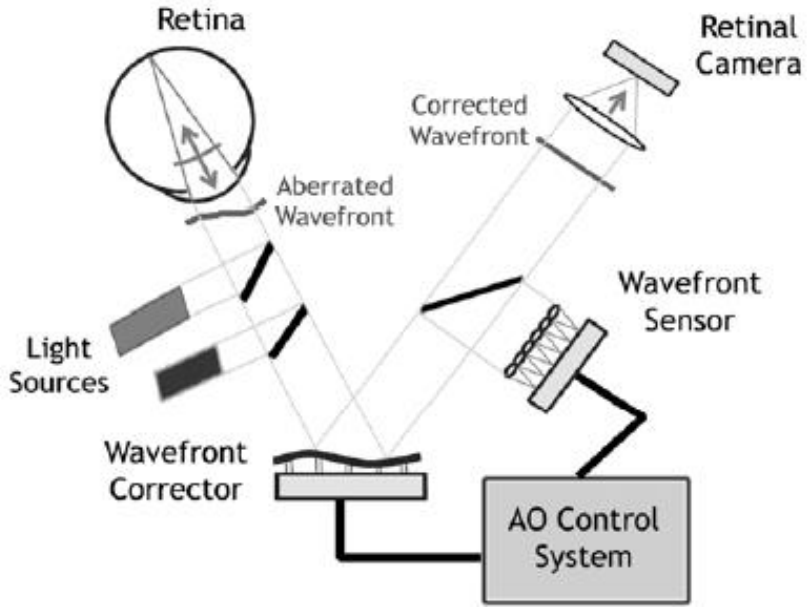

Figure 1.8. Basic layout of an adaptive optics system for retinal imaging. The system measures the ocular aberrations with a wavefront sensor and corrects for them with a wavefront corrector to achieve high lateral resolution imaging. Two light sources are generally used by an AO system: one is used to measure and correct the wavefront aberration of the eye; the second source is used to illuminate the retinal field being imaged. The AO compensated retinal image is captured by a high-resolution imaging camera [1].

AO systems operating in closed-loop place the wavefront sensor after the wavefront corrector. In this configuration, the measured wavefront is the error signal that gets fed back to the controller to further reduce the residual aberrations in the next iteration, theoretically correcting the retinal images up to the diffraction limit.

1.6 rtx1; Adaptive Optics Retinal Camera

In this work, the sequences of retinal images are obtained using a commercial AO-assisted flood illumination system; the rtx1 from Imagine Eyes, France as shown in Figure 1.9 [17, 18].

Figure 1.9 Rtx1 AO retinal camera by Imagine Eyes, France, (image from http://www.imagine-eyes.com/imagine-eyes-many-thanks-to-presenters-at-the-rtx1-e-workshop/).

The rtx1 has seven different optical paths; 4 for illumination, 1 for analysis and 2 for imaging. The illumination and imaging system of rtx1 are shown in Figures 1.10 and 1.11 respectively.

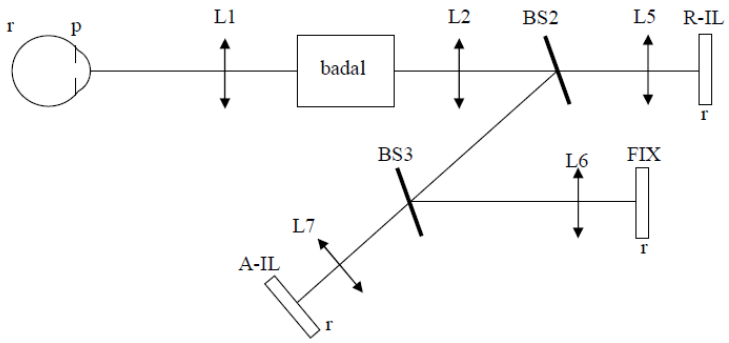

Figure 1.10 Illumination system of the rtx1 retinal camera (where r is retina, p is pupil, L is lenses, badal optometer, BS is the beam splitters, R-IL is the illumination source for the retinal imaging, FIX is the fixation target and A-IL is the illumination source for wavefront sensing) [18].

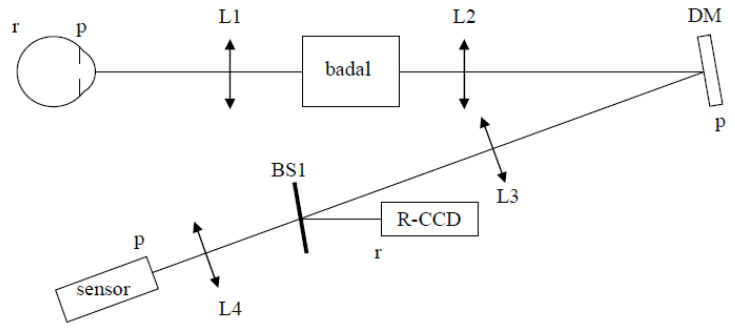

Figure 1.11 Imaging system of the rtx1 retinal camera (where r is retina, p is pupil, L is lenses, Badal optometer, DM is the deformable mirror, CCD is the scientific camera for retinal imaging, BS is beam splitters and sensor is the wavefront sensor) [18].

In the rtx1 retinal imaging illumination system, to provide a uniform illumination field on the retina an 850 nm LED (R-IL) is used. By a 750 nm super luminescent diode (SLD) (A-IL), a point source on the retina, for wavefront sensing, is created, and an array of ten 950 nm LEDs are used to uniformly illuminate the iris. As a fixation target on the retina, an internal organic light emitting diode (OLED) miniature monitor (FIX) is used.

In the rtx1 retinal imaging system, a low noise CCD camera (R-CCD) (Rooper Scientific) with 1392 x 1040 pixels is used to image the 4°x 4° area of the retina, which corresponds to approximately 1.2 mm x 1.2 mm in the retina for an emmetropic eye. Here, one camera pixel is equivalent to 1.6 µm in the retina. The rtx1 uses a continuous magnetic deformable mirror *mirao52e* (Imagine Eyes, France) which provides a maximum ±50 µm stroke to correct for the aberrations present in almost any eye. In this deformable mirror, the magnets are glued under the continuous membrane of the mirror and set above coils. When voltage is applied to the coils, they generate magnetic fields which push or pull the magnets. Here, the 52 actuators are placed in an ~ 17 mm diameter area where the mirror surface covers an area of 15 mm diameter.

The pupil imaging used for patient alignment is using a standard CCD (Allied vision) camera with 656 x 494 pixels mounted with a standard objective (Pentax) with a focal length of 35 mm. In addition, each of the optical paths except for pupil illumination and imaging, has a badal system to compensate for the eye ametropia from -10 D to + 8 D, leaving the deformable mirror stroke fully available to compensate for astigmatism up to 5D, strong eye optical defects and to focus the image at different layers of the retinal microstructure.

The rtx1 imaging system requires 9 ms exposure time. The total acquisition time for the 40 frames is approximately 4 seconds with 105 ms of interval time between the frames [18].

The full exam including patient alignment and post-processing takes a few minutes per eye for most patients, making it suitable for use in large-scale clinical studies.

The AO retinal camera, rtx1, allows to resolve numerous structural aspects of the living human retina by the direct visualization of photoreceptors, retinal vessels and nerve fiber bundles. The photoreceptor cells represent the study primary target for many research groups. Due in part to the optical waveguide properties of photoreceptors, the cone mosaic can be imaged easily (Figure 1.12), and furthermore, many retinal diseases involve cones losses.

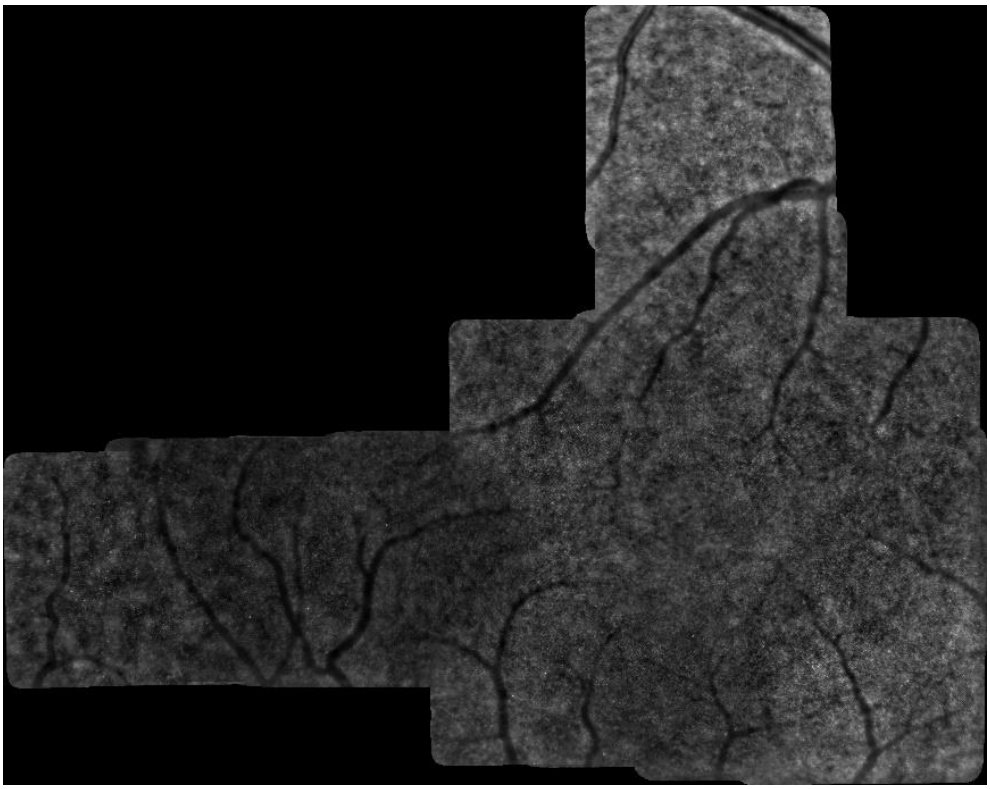

Figure 1.12. Example of rtx1 AO image montage form a healthy 29 year old female subject.

1.7 The Photoreceptor Mosaic and degenerative diseases of the human retina

The arrangement of the photoreceptor types in the retina is well described histologically [19,20]. The cone and rod photoreceptors are closely packed, forming a patterned appearance, or mosaic. Rods substantially outnumber cones over the entire retina. In the

developing human retina, the relative distribution of cone and rod photoreceptors is roughly constant; that is, a 20:1 ratio is maintained across the entire retina. However, across an adult retina, the ratio of rods to cones varies substantially. The adult fovea contains the highest density of cone photoreceptors, enabling high acuity vision.

However, the density of cone photoreceptors quickly falls off as a function of distance from the fovea, yielding to a high density of rod photoreceptors, which peaks at about 10 degrees from the fovea (Figure 1.13).

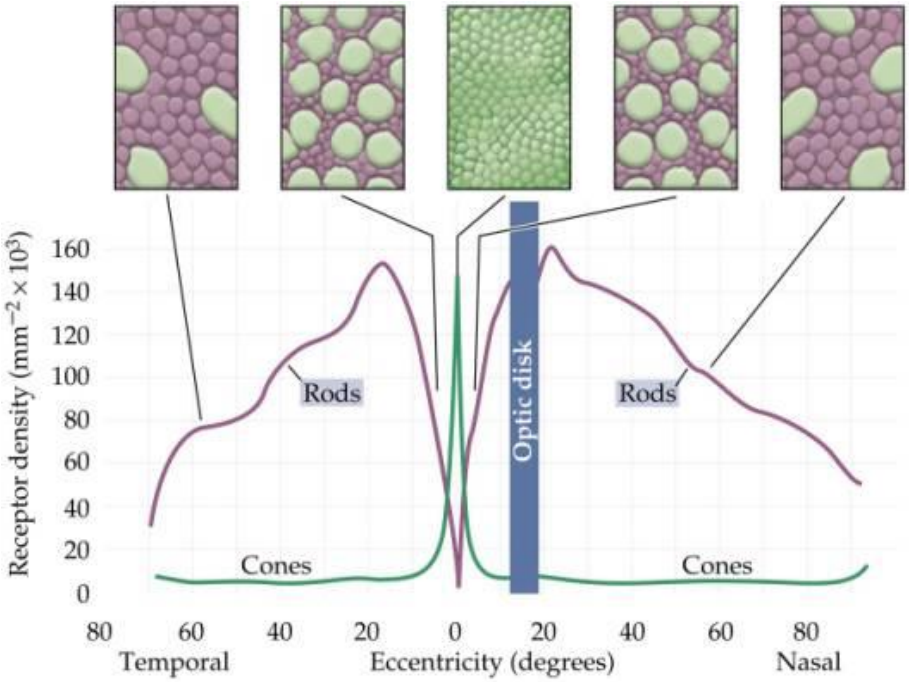

Figure 1.13 Rods (in violet) and cones (in green) are distributed regionally: in the Center of the eye (i.e., the fovea) there are only cones; in the Peripheral retina, mainly rods and few cones. (Image from the web site http://www.rci.rutgers.edu/~uzwiak/AnatPhys/Vision.htm)

In some eye diseases, the retina becomes damaged or compromised, and degenerative changes set in that eventually lead to serious damage to the nerve cells that carry the vital messages about the visual image to the brain. Many inherited and acquired retinal diseases are associated with disruption or alteration of photoreceptor structure and function, including Best vitelliform macular dystrophy, retinitis pigmentosa, Usher syndrome, cone-rod dystrophy, age-related macular degeneration, and diabetic retinopathy (Figure 1.14).

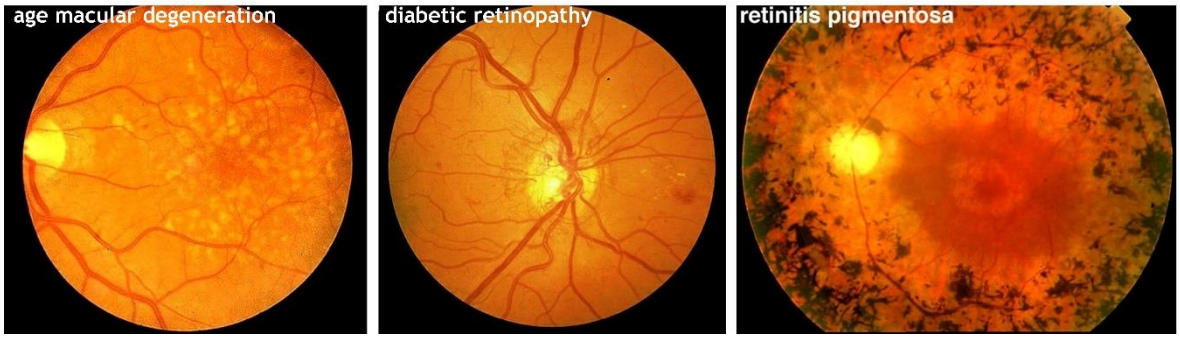

Figure 1.14 A view of the fundus of the eye and of the retina in patients who have acquired and inherited retinal diseases [21].

These pathologies are typically tracked using clinical instruments which have resolution limited to gross retinal structures, thereby limiting the ability to effectively track disease progression at cellular level.

Adaptive optics (AO) ophthalmoscopy can be applied to assess these pathologies with very high resolution, allowing a finer view of retinal disease progression [22], Figure 1.15.

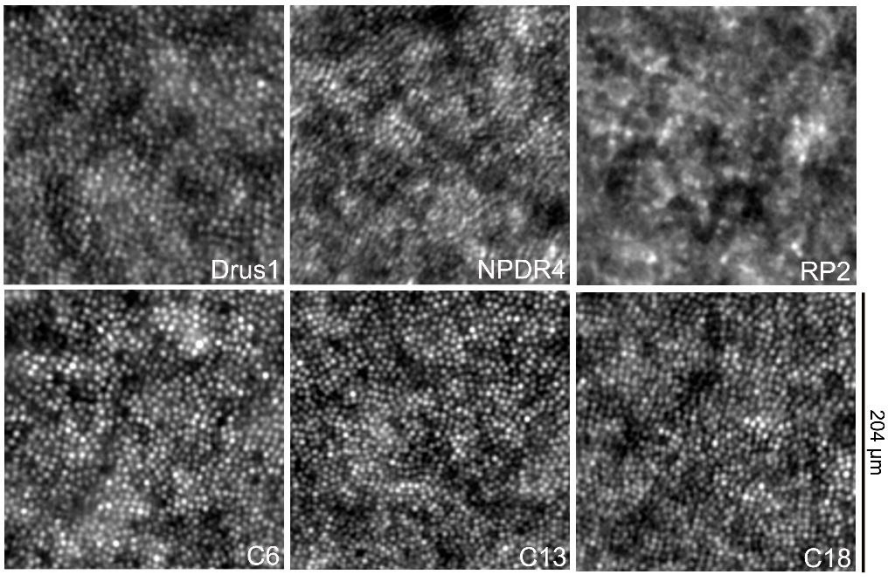

Figure 1.15. Adaptive optics images of the parafoveal cone mosaic in patients with retinal diseases and healthy subjects acquired at 1.5 degrees superior from the fovea. Up: the photoreceptor mosaic showed variable cell loss and abnormalities in the packing arrangement of the cones with respect to healthy subjects (down).

1.8 Summary of dissertation aim

The assessment of the structure of the photoreceptor mosaic in AO images needs methods to quantify the arrangement of the cells. For this purpose, a variety of geometric and statistical algorithms were developed to analyse the coordinates identifying the position of cone centroids. In particular, the most used metrics are cell density, the percentage of six-sided Voronoi cells and spacing metrics.
The aim of this thesis is to study the arrangement of the parafoveal cone mosaic from AO flood illumination images with two different approaches:

1. The first approach is a global analysis of the spacing between cones by extraction of three frequently used spacing metrics;
2. The second approach is a local pointwise analysis of the tendencies of the cones for aggregation and repulsion at specific distance, by statistical point pattern analysis.

First, Chapter 2 explores the relationship between in-use spacing metrics of photoreceptor structure and how each is affected by changes in retinal eccentricity and window sample size. This chapter deals with the introduction and the assessment of three spacing metrics, the center-to-center spacing (S_{cc}), the local cone spacing (LCS), and the Density Recovery Profile Distance (DRPD) frequently used to evaluate the distribution of cell distances in adaptive optics (AO) images of the cone mosaic.

Chapters 3 focus on the application of new approaches for measuring photoreceptor arrangement by spatial point pattern analysis. Here we used statistical second order descriptors to characterize the spatial distributions of photoreceptors in real and simulated images. These spatial descriptors include the pair correlation function $g_2(r)$, the structure factor s(k) and various nearest neighbor second order statistics (G(r), K(r) and L(r)), to quantify the reciprocal influence of the cells at a variable distance r.
Finally, starting from the results of the previous spatial point pattern analysis, the aim of Chapter 4 is evaluating dissimilarities profiles of the individual spatial second order functions, seen in the previous chapter 3, extracted from the control and diseased groups, for partitioning individual curves into homogeneous classes.

Chapter 2

Reliability and agreement between metrics of cone spacing in adaptive optics images of the human retinal photoreceptor mosaic

2.1 Introduction

Adaptive optics (AO) retinal imaging has enabled direct visualization of the cone mosaic and measurement of density, spacing and packing arrangement of cones in normal eyes and eyes with retinal diseases [23,24]. Since an increasing number of studies is providing descriptive information about the integrity and pathological change of the retinal cone mosaic using various approaches, it is of clinical importance to understand whether the results from different studies can be reliably compared [25,29]. In previous work [30,31], we have evaluated the agreement of density and packing arrangement of cones between sampling areas of different size and geometry. The results from normal eyes have shown that caution is needed when comparing cone density evaluated in sampling areas of different sizes (the average difference can reach 10% between 320x320 μm and 64x64 μm sampling windows) [30,31]; the packing arrangement of cones by Voronoi analysis has been shown to be minimally affected by window size. To construct a Voronoi, each cone, identified by its geometrical centroid, corresponds to a Voronoi tile that is color coded with respect to their cones neighbors. The primary advantages and drawbacks of these metrics have been previously discussed [1,26,27,30,31]. Cone density analysis creates strict demands on image quality because it requires that all cones within the region of interest be identified. For this reason, manual inspection of the cones in each image is highly recommended in order to minimize errors [1,26,30,31]. In addition, the moderate to high variability of cone density even in healthy adults may make this metric insensitive to small deviations from normal [1,29]. The limit of Voronoi analysis is related to the accuracy of the cone identification algorithm, the manual re-selection of the unidentified or misidentified cones, and the *boundary effect* which is an apparent distortion of the Voronoi mosaic due to the exclusion of cones beyond the sampling window, the effect of which increases as the sampling window decreases [30,31]. It has been previously shown that the cone detection algorithm which segments the cone aperture, rather than only identifying the cone centroid position, is the most accurate approach for identifying the cones [32,33].

Despite broad use of spacing metrics in clinical studies, there have been few evaluations of the reliability and agreement among various metrics.[13] Overall, cone spacing analysis is less affected by image quality variations than cone density, because these methods do not require identification of every cone within the region of interest [1,25,26,28,35]. For this reason, spacing metrics can be less prone to errors than cone density when tracking disease progression or response to treatment in eyes with retinal diseases, in which cones may be poorly imaged due to loss of wave-guiding property or missing cells [25]. However, there is

no supporting evidence that cone spacing metrics alone may provide a robust measurement for comparison among eyes (or even the same eye over time) in clinical studies [1,25,34,35]. The majority of studies have used two main methodologies to estimate the spacing of cells in AO images of the cone mosaic; the density-count method and the distribution-of-distances methods. The center-to-center spacing (S_{cc}) is a measure that has been frequently adopted in studies of cone photoreceptor mosaic [36,37,38]. The S_{cc} is based on the density count method, which is derived from the number of cones per unit area. The distribution-of-distances methods are assumption free and provide estimates of both central tendency and variation. These methods include the nearest neighbour distance (NND), the local cone spacing (LCS), and the nearest-neighbour cone spacing extracted from the Density Recovery Profile (DRP), which has been recently termed Density Recovery Profile Distance (DRPD) [19,34,39,40].

The scope of the present work was to assess the reliability and agreement of three spacing metrics, such as S_{cc}, LCS and DRPD, for evaluating the distribution of cell distances in AO flood illumination images of the parafoveal cone mosaic. The metrics were calculated over two different sampling areas to evaluate the effect of window size on cone spacing estimates. In order to evaluate the influence of cell reflectivity loss and cone packing arrangement abnormalities on spacing metrics, the dataset included AO images acquired from healthy adult subjects and patients with a diagnosis of acquired or inherited retinal diseases.

2.2 Methods

All research procedures described in this work adhered to the tenets of the Declaration of Helsinki. The protocol was approved by the local ethical committee (Azienda Sanitaria Locale Roma A, Rome, Italy) and all subjects recruited gave written informed consent after a full explanation of the procedure. Inclusion criteria were age >18 years old, no previous eye surgery, eye inflammation, glaucoma or cataract; in addition, control subjects were required to have no history or presence of systemic diseases. Subjects recruited for the study received a complete eye examination, including non-contact ocular biometry using the *IOL Master* (Carl Zeiss Meditec Inc, Jena, Germany).

Table 2.1. Characteristics of study participants.

Participants	***Age*** (years)	***Gender***	***AxL*** (mm)*	***SEr*** (D)*	RMF_{corr} (mm/deg^2)*
Healthy subjects					
C_1	52	F	24.73	-0.5	0.294
C_2	37	F	25.49	-4.7	0.303
C_3	24	F	25.06	-2.7	0.298
C_4	32	M	27.04	-6.2	0.322
C_5	33	F	23.60	0.0	0.281
C_6	27	M	23.58	-2.5	0.281
C_7	40	M	22.61	0.0	0.269
C_8	26	F	26.29	-5.2	0.313
C_9	24	F	21.66	-1.2	0.258
C_10	36	F	25.67	-5.2	0.306
C_11	39	F	22.11	0.2	0.263
C_12	37	F	22.11	0.5	0.263
C_13	29	F	24.42	-2.2	0.291
C_14	24	F	24.38	-3.7	0.290
C_15	23	F	25.34	-3.5	0.302
C_16	36	F	23.98	-5.1	0.285
C_17	54	F	24.73	-0.5	0.294
C_18	23	F	24.53	0.0	0.292
C_19	46	M	23.50	0.2	0.280
C_20	33	M	23.69	0.0	0.282
M±SD	***33 ± 9***		***24.23±1.42***	***-2.1±2.3***	***0.200±0.017***
Retinal diseases					
Drusen_1	38	M	24.03	-0.2	0.286
Drusen_2	42	F	25.40	-0.5	0.302
NPDR_1	51	F	24.77	-1.5	0.295
NPDR_2	38	F	23.80	0.0	0.283
NPDR_4	33	M	26.34	-4.2	0.314
NPDR_5	35	F	21.89	0.0	0.261
Best	56	F	24.07	-0.5	0.286
OMD	23	F	25.57	-2.0	0.304
RP_1	46	F	24.50	-1.0	0.292
RP_2	40	F	23.20	0.0	0.276
RP_3	42	F	22.62	1.0	0.269
RP_4	59	F	22.81	1.0	0.271
M±SD	***41± 10***		***24.08±1.32***	***-0.7±1.4***	***0.287±0.016***

****Axl***=axial length; ***SEr***= manifest spherical equivalent refraction; RMF_{corr}= corrected magnification factor.

2.2.1 Human subjects

Twenty healthy volunteers (age 33± 9 years old; range 23-54 years; gender: 15 F and 5 M), and twelve patients with retinal diseases (age 41±10 years old; range 23-59 years; gender: 10 F and 2 M) were recruited in this study (Table 2.1). The latter participants included subjects with a diagnosis of diffuse cuticular drusen and a family history of age-related macular degeneration (Drusen; n=2) [41,42], non proliferative diabetic retinopathy (NPDR;

n=4) according to the ETDRS severity scale [43,44], retinitis pigmentosa (RP; n=4; USH2A gene mutation), Best macular dystrophy (Best; n=1; BEST 1 gene mutation) and occult macular dystrophy (OMD; n=1; RP1L1 gene mutation) [45].
These participants were enrolled in this study in order to have a dataset of AO images of the cone mosaic with increasing amount of cell loss and variable abnormalities in the packing arrangement of the cones.

2.2.2 Image acquisition and processing

A flood-illuminated AO retinal camera (*rtx1*, Imagine Eyes, France) was used to collect images of the cone mosaic on 20 healthy subjects and 12 subjects with various retinal diseases. The imaging session was conducted after dilating the pupil with one drop of 1% tropicamide. During imaging, fixation was maintained by instructing the patient to fixate on the internal target of the instrument moved by the investigator. At each retinal location, a sequence of 40 frames (rate: 9.5 frames/sec) was acquired by illuminating a retinal area subtending 4 degrees of visual angle in the right eye of each subject; images were acquired at several locations in the central retina covering an area of 5x4 degrees centered on the preferred locus of fixation (PRL, coordinates x=0° and y=0° and here used as the foveal reference point).
A proprietary program from the manufacturer has been used to correct for distortions within frames of the raw image sequence and to register and frame-average to produce a final image with enhanced signal-to-noise ratio prior to further analysis. In this study, two sampling areas of different size (64x64 µm and 204x204 µm) were cropped from each final image at 1.5 degrees superior and 2.5 degrees temporal from the PRL. The two eccentricities were chosen to be a compromise between the resolution limit of the instrument, which does not allow all the cones to be resolved too close to the fovea, and the presence of rods, which alter the cone relative spacing enough to be detectable by the instrument when further than 4 degrees from the fovea.
The nonlinear formula of Drasdo and Fowler and the Gullstrand schematic model eye parameterized by the biometry measurements (corneal central curvature, anterior chamber central depth, axial length) were used to convert each final image from degrees of visual angle to micrometers on the retina [46,47]. The corrected magnification factor (RMF_{corr}) was calculated for each eye in order to correct for the differences in optical magnification and thus retinal image size between eyes, as previously described [30,31,44-47].

Image cone labelling was automatically performed using an enhanced version of the algorithm implemented with the image processing toolbox in Matlab (The Mathworks Inc, Natick MA, USA) [30,31,43,44,48]. Cones were identified independently in each sampling window. The cone identification algorithm's performance was verified by three expert investigators (DG, LM, ML), who reviewed each sampling area and manually identified cones that they agreed to be missed or selected in error by the algorithm. This procedure ensured that the number of excluded cones was minimised. A buffer zone was created in each sampling window in order to minimize the *boundary effect* for packing geometry metrics [30.31]. The *x*,*y* coordinates of the cones in each sampling window were then stored in a text array and used to calculate the cone metrics.

2.2.3 Density and packing arrangement metrics of the cone mosaic

Cone counts were converted into local densities by calculating their number per square millimeter (cones/mm^2). The cone packing arrangement was analyzed using Voronoi diagrams [30,31,49,50]. The Voronoi tessellation was implemented by the *voronoi* Matlab function from the bidimensional coordinates of labelled cones, as previously described [30,31,44,49]. The Voronoi regions lying at the bounds of each section were excluded from further analysis, creating a buffer zone = 2 NND in order to minimize the *boundary effect*. The number of Voronoi tiles with six sides (6*n*) was divided by the total number of bound Voronoi tiles within each sampling area and expressed as a percentage.

2.2.4 Spacing metrics of the cone mosaic

Three metrics were used to describe the distribution of cone distances:

1. The center-to-center spacing (S_{cc}) was determined from cone density using the following expression:

$$S_{cc} = 1000\left[\frac{2}{\sqrt{3}D}\right]^{1/2} \quad (2.1)$$

where D is the number of cones per square millimeter. Since the method assumes an exact relationship between cone density and spacing, the cones are expected to be arranged in triangular lattice (this metric was also termed minimum center-to-center

spacing) [36-38,49]. It is equivalent to the metric *S* used by Chui et al. [36] and *S(x,y)* used by Li et al. [37]. Care should be taken to avoid regions of missing data (e.g., large blood vessels, image boundary etc.) or defects in the image in order to avoid overestimating the spacing distribution of cones.

2. The local cone spacing (LCS) was determined by calculating the average of the minimum distances from the center of a given cone to the centers of six neighboring cones within an area of 12 pixels (9.6 μm) diameter (i.e., almost twice the size of the cone at both retinal locations) [44]. The LCS has been developed in order to minimize the known limits of NND in estimating the mosaic spacing. Indeed, the NND takes into account only the nearest of each cell's known neighbours, regardless of its distance; therefore, it can be strongly influenced by very large NNDs of isolated cells, which decrease its sensitivity to represent the distribution of cell distances in retinal diseases [34].
3. The density recovery profile distance (DRPD) was derived from the DRP reconstructed from the autocorrelogram [39]. The spatial autocorrelogram was generated by superimposing the distribution of all cells in a sampling area using each cell in the area in turn as the reference cell. In order to determine the nearest-neighbour cone distance, the DRPD was calculated as the first local maximum of the Density Recovery Profile created from the autocorrelogram with max radius = 1/5 of the image dimension and a series of annuli of 1 μm width. The width of each bin was determined from equation 16 in Rodieck et al. [39], under assumption of having a reliability factor value of 5 and 4 for healthy subjects and patients with retinal diseases, respectively. The bin's width was accordingly 1 μm in the two populations. The DRPD takes into account all of a cell's neighbours up to a limited distance that depends on the shape of the DRP, which is a graphical representation of spatial behaviour derived from the spatial autocorrelogram [39]. It is equivalent to the nearest-neighbour cone spacing determined from the DRP in previous studies [25,35]. Nevertheless, the DRP provides a different measure than the nearest neighbour distance and a more complete overview of the spatial arrangement of the cone mosaic; its estimates are based upon all of the other points about a given point, rather than just one.

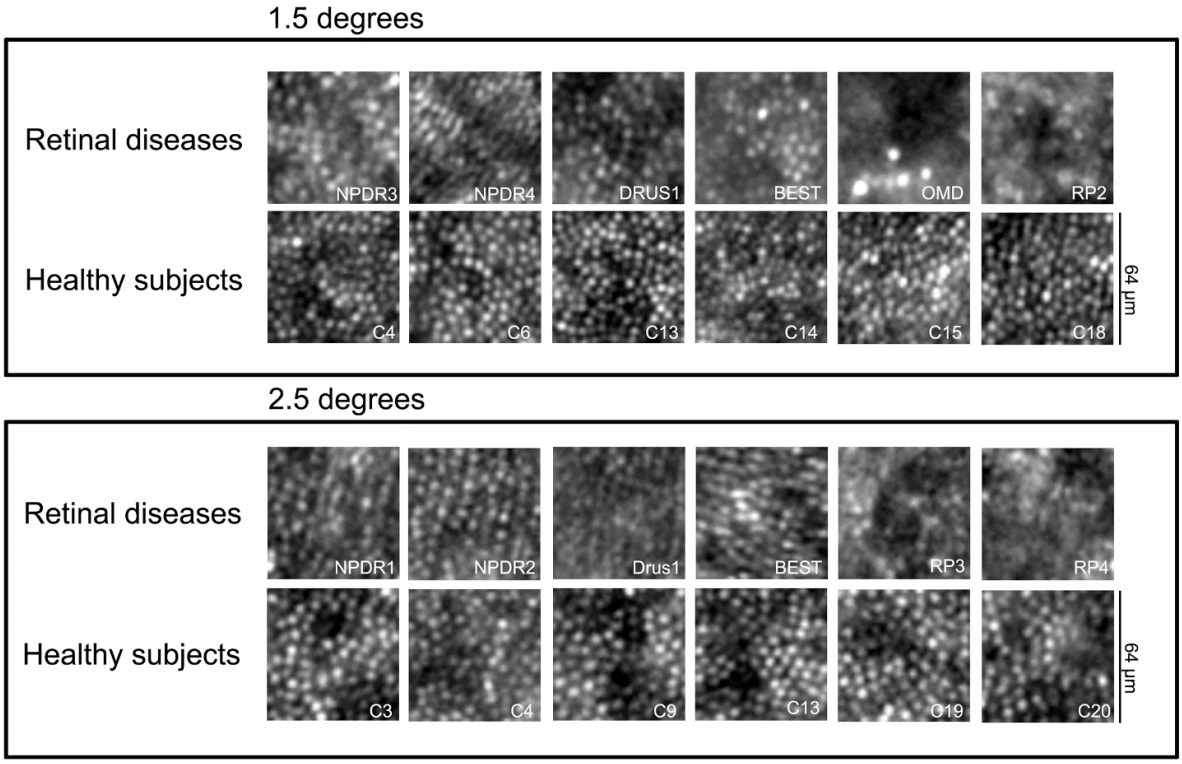

Figure 2.1 - Adaptive optics images of the parafoveal cone mosaic in patients with retinal diseases and healthy subjects acquired at 1.5 degrees superior and 2.5 degrees temporal from the fovea. The photoreceptor mosaic in patients with retinal diseases showed variable cell loss and abnormalities in the packing arrangement of the cones with respect to healthy subjects. The sampling area subtends 64x64 µm. Data from participants are summarized in table 2.1.

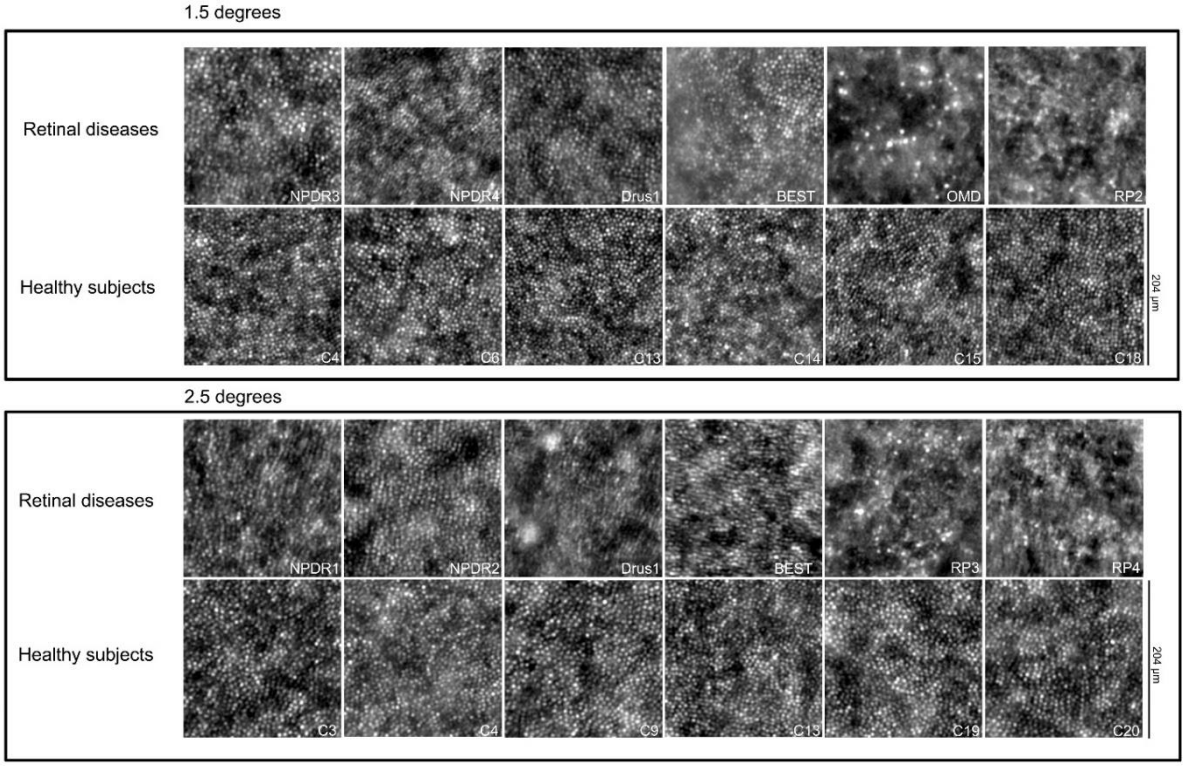

Figure 2.2 - Adaptive optics images of the parafoveal cone mosaic in patients with retinal diseases and healthy subjects acquired at 1.5 degrees superior and 2.5 degrees temporal from the fovea. The sampling area subtends 204x204 µm. Data from participants are summarized in table 2.1.

2.2.5 Statistics

Data were expressed as mean ± standard deviation. Statistics were performed using the SPSS software (version 17.1; SPSS Inc., Chicago, IL USA) and Matlab (version R2013a, The Mathworks Inc., Natick MA, USA).

The sample size was calculated to detect a mean difference in cone density of 2500 cones/mm^2 (SD = 2500 cones/mm^2) between healthy subjects and patients with retinal diseases (2:1 allocation) with a two-sided significance level of 5% and a power of 82%.

The intraclass correlation coefficient (ICC; two-way, random effects model) was calculated in order to estimate the absolute agreement between each pair of spacing metrics in the two sampling areas for each study group. The correlation and Bland-Altman analysis were used to assess the 95% limits of agreement (LoA) between the pair of spacing metrics that have shown high absolute agreement (ICC>0.7), and between the values of each spacing metric extracted from the two sampling areas. The differences between the spacing metrics of the two study groups was evaluated using the non-parametric Mann Whitney U test.

2.3 Results

2.3.1 Cone density and packing arrangement

Over a 64x64 µm sampling area, the cone densities at 1.5 degrees and 2.5 degrees retinal eccentricities in healthy subjects were 32281±2281 cones/mm^2 and 29411±2147 cones/mm^2, respectively (Figure 2.1). Cone density in patients with retinal diseases was on average 26±3% (range from 2% to 65%; P<0.001) lower than in healthy subjects.

Over a 204x204 µm sampling area, the cone densities at 1.5 degrees and 2.5 degrees from the PRL in healthy subjects were 31494±2489 cones/mm^2 and 28703±1822 cones/mm^2, respectively (Figure 2.2). Cone density in patients with retinal diseases was on average 16±5% (range from 1% to 58%; P<0.001) lower than that in healthy subjects.

The average percentage of six-sided Voronoi tiles was almost constant across different sampling areas in either study groups. In healthy subjects, the 6*n* Voronoi average ranged from 50% to 45% for 1.5 degrees and 2.5 degrees, respectively. In patients with retinal diseases, the average 6*n* Voronoi tiles were significantly lower than control values (P<0.05), except for values calculated in 204x204 µm sampling areas at 2.5 degrees retinal eccentricity (P=0.14). Cone density and percent of six-sided Voronois for all cases are shown in table 2.2.

Table 2.2. Mean (±*SD*) cone density and percentage of six-sided (6*n*) Voronois in study participants over different sampling areas at two retinal locations.

Sampling area	**64 µm x 64 µm**				**204 µm x 204 µm**			
Metric	Cone density (cones/mm^2)		6*n* Voronois (%)		Cone density (cones/mm^2)		6*n* Voronois (%)	
Retinal eccentricity	1.5 degrees	2.5 degrees	1.5 degrees	2.5 degrees	1.5 degrees	2.5 degrees	1.5 degrees	2.5 degrees
Healthy subjects								
C_1	30476	26905	51.1	47.3	29924	27438	48.7	43.2
C_2	36341	30732	57.0	46.5	35517	30154	57.1	48.1
C_3	29286	26429	48.2	45.3	27683	26591	51.5	45.9
C_4	31951	28780	55.9	45.6	31707	28331	55.7	48.0
C_5	34146	33659	47.0	40.8	33397	32153	47.0	42.4
C_6	28537	30976	59.3	45.6	27632	29587	53.0	41.7
C_7	31951	29024	43.0	40.9	30431	27392	39.1	45.5
C_8	32927	28780	41.8	51.2	34880	27861	47.3	48.4
C_9	31220	28537	48.9	32.5	29021	27375	48.2	39.7
C_10	36098	30732	50.9	43.0	34641	29139	48.7	48.0
C_11	34146	28537	44.5	40.7	31599	27446	43.8	40.0
C_12	32195	26585	41.8	44.8	31367	29305	44.1	41.6
C_13	34878	29512	57.6	50.0	33861	27387	54.5	53.9
C_14	35366	27561	58.2	50.6	34053	26595	52.5	52.7
C_15	32927	27805	60.4	44.9	34378	27081	53.2	47.2
C_16	30488	30488	44.8	46.0	30571	30476	42.2	46.1
C_17	30000	29756	39.3	39.3	28490	28727	51.1	44.4
C_18	30000	34390	59.5	53.0	29333	32952	51.6	46.1
C_19	30732	27805	40.5	48.7	29986	27374	38.0	45.3
C_20	31951	31220	54.4	39.1	31411	30694	51.1	40.9
M*±*SD	***32281*±*2281***	***29411*±*2147***	***50.3*±*7.0***	***44.8*±*4.9***	***31494*±*2489***	***28703*±*1822***	***48.9*±*5.3***	***45.5*±*3.9***
Retinal diseases								
Drusen_1	24146	27317	48.5	44.2	22679	28900	50.1	43.4
Drusen_2	24390	28780	41.2	49.4	27524	28762	42.9	41.5
NPDR_1	26341	23902	39.2	34.4	26571	24000	47.5	47.9
NPDR_2	26098	23171	44.4	47.6	26738	23452	42.9	46.6
NPDR_4	31707	24146	34.8	47.7	32110	25396	47.9	46.4
NPDR_5	24146	25122	48.4	36.6	24442	23444	43.2	43.5
Best	23500	25750	58.1	34.8	25444	24412	45.6	48.8
OMD	11463	10244	44.0	31.8	13134	16914	35.5	33.4
RP_1	19024	17073	43.7	30.2	26754	27112	41.2	39.1
RP_2	24146	23902	47.6	35.9	25273	27411	39.1	41.7
RP_3	25366	21951	41.4	37.9	26850	25298	41.0	39.3
RP_4	19512	18293	32.6	34.7	25273	26247	41.7	41.3
M*±*SD	***23320*±*4937***	***22471*±*5089***	***43.7*±*6.8***	***38.8*±*6.7***	***25233*±*4422***	***25112*±*3203***	***43.2*±*4.1***	***42.7*±*4.4***
P value	***<0.001***	***<0.001***	***0.02***	***0.01***	***<0.001***	***<0.001***	***0.003***	*0.14*

2.3.2 Cone spacing metrics

In healthy subjects, the values of all spacing metrics increased with increasing eccentricity and showed high consistency between the two different sampling areas; S_{cc} ranged from 5.99±0.21 μm to 6.35±0.24 μm from 1.5 degrees to 2.5 degrees from the fovea respectively; LCS ranged from 6.12±0.18 μm to 6.41±0.18 μm respectively; and DRPD ranged from 5.80±0.80 μm to 6.20±0.66 μm respectively. In patients with retinal diseases, the spacing metrics showed higher variation around the mean values, which was caused by the abnormal and variable distribution of distances between cells across the parafoveal retinal locations in the disease population (Table 2.3).

The differences of S_{cc} and LCS values between healthy subjects and patients with retinal diseases were statistically significant ($P \leq 0.01$) in both sampling areas at both retinal eccentricities, except for the LCS values measured in the 204x204 μm area at 2.5 degrees retinal eccentricity (P=0.27). This result was consistent with the distribution of 6*n* Voronois between healthy and pathologic cases in the same area (see Table 2.2). The differences of DRPD values between healthy subjects and patients with retinal diseases were not statistically significant in any case.

2.3.2.1 Agreement and correlation between spacing metrics

The S_{cc} and LCS values showed high agreement with each other in healthy subjects over both sampling areas and both retinal eccentricities (averaged ICC=0.86; ICC range=0.80-0.93). On the other hand, the agreement between S_{cc} and LCS values in patients with retinal diseases was poor (averaged ICC=0.28; ICC range=0.08-0.51). The agreement between the DRPD and the other two spacing metrics was low in both study groups (averaged ICC=0.27; ICC range=0.05-0.47). The ICC analysis between each pair of spacing metrics is summarized in Table 2.4.

Table 2.3. Mean (±*SD*) values of the three spacing metrics in different sampling areas at two retinal locations.

Sampling area	**64 µm x 64 µm**						**204 µm x 204 µm**					
Metric	S_{cc} (µm)		LCS (µm)		DRPD (µm)		S_{cc} (µm)		LCS (µm)		DRPD (µm)	
Retinal eccentricity	1.5 deg	2.5 deg	1.5 deg	2.5 deg	1.5 deg	2.5 deg	1.5 deg	2.5 deg	1.5 deg	2.5 deg	1.5 deg	2.5 deg
Healthy subjects												
C_1	6.16	6.55	6.22	6.57	5.50	6.50	6.21	6.49	6.29	6.46	5.50	6.50
C_2	5.64	6.13	5.86	6.31	5.50	6.50	5.70	6.19	5.82	6.25	5.50	5.50
C_3	6.28	6.61	6.39	6.65	6.50	6.50	6.46	6.59	6.51	6.59	5.50	6.50
C_4	6.01	6.33	6.07	6.43	5.50	5.50	6.03	6.38	6.12	6.45	5.50	6.50
C_5	5.82	5.86	5.90	6.05	5.50	5.50	5.88	5.99	5.96	6.08	5.50	5.50
C_6	6.36	6.11	6.09	6.38	5.50	5.50	6.46	6.25	6.26	6.53	5.50	5.50
C_7	6.01	6.31	6.41	6.28	6.50	6.50	6.16	6.49	6.50	6.31	6.50	6.50
C_8	5.92	6.33	6.01	6.38	5.50	6.50	5.75	6.44	5.86	6.50	5.50	6.50
C_9	6.08	6.36	6.18	6.52	6.50	5.50	6.31	6.49	6.36	6.52	6.50	6.50
C_10	5.66	6.13	5.89	6.40	4.50	5.50	5.77	6.30	5.86	6.42	5.50	5.50
C_11	5.82	6.36	6.07	6.95	5.50	6.50	6.05	6.49	6.15	6.51	6.50	6.50
C_12	5.99	6.59	6.08	6.63	5.50	6.50	6.07	6.28	6.17	6.36	5.50	6.50
C_13	5.75	6.26	5.92	6.43	5.50	5.50	5.84	6.49	5.96	6.60	5.50	5.50
C_14	5.71	6.47	5.89	6.61	5.50	5.50	5.82	6.59	5.91	6.65	5.50	5.50
C_15	5.92	6.44	6.07	6.38	5.50	7.50	5.80	6.53	5.90	6.55	5.50	6.50
C_16	6.15	6.15	6.33	6.27	6.50	5.50	6.15	6.16	6.20	6.24	6.50	5.50
C_17	6.20	6.23	6.37	6.46	5.50	7.50	6.37	6.34	6.42	6.37	5.50	6.50
C_18	6.20	5.79	6.28	5.91	5.50	6.50	6.27	5.92	6.34	5.99	5.50	5.50
C_19	6.13	6.44	6.31	6.53	8.50	6.50	6.21	6.49	6.25	6.52	8.50	6.50
C_20	6.01	6.08	6.11	6.27	5.50	6.50	6.06	6.13	6.14	6.24	5.50	6.50
M±SD	***5.99± 0.21***	***6.28± 0.22***	***6.12± 0.18***	***6.42± 0.22***	***5.80± 0.8***	***6.20± 0.66***	***6.07± 0.24***	***6.35± 0.19***	***6.15± 0.22***	***6.41± 0.18***	***5.85± 0.75***	***6.10± 0.5***
Retinal diseases												
Drusen_1	6.92	6.50	6.91	6.57	5.50	5.50	7.14	6.32	7.01	6.32	6.50	5.50
Drusen_2	6.88	6.33	6.64	6.31	5.50	4.50	6.48	6.34	6.33	6.29	5.50	5.50
NPDR_1	6.62	6.95	6.55	6.82	6.50	6.50	6.59	6.94	6.59	6.83	5.50	6.50
NPDR_2	6.65	7.06	6.56	6.88	6.50	5.50	6.57	7.02	6.54	6.86	6.50	6.50
NPDR_4	6.03	6.92	6.08	6.81	5.50	6.50	6.00	6.74	6.02	6.73	5.50	6.50
NPDR_5	6.92	6.78	6.74	6.59	6.50	6.50	6.87	7.02	6.65	6.79	6.50	6.50
Best	7.01	6.70	6.94	6.61	6.50	6.50	6.74	6.88	6.67	6.70	6.50	6.50
OMD	10.04	10.62	6.91	6.48	6.50	4.50	9.38	8.26	6.59	6.38	6.50	4.50
RP_1	7.79	8.22	6.62	6.56	4.50	4.50	6.57	6.53	6.26	6.14	5.50	4.50
RP_2	6.92	6.95	6.69	6.34	6.50	4.50	6.76	6.49	6.47	6.34	5.50	5.50
RP_3	6.75	7.25	6.50	6.70	5.50	7.50	6.56	6.76	6.36	6.46	6.50	5.50
RP_4	7.69	7.95	6.60	6.61	5.50	4.50	6.76	6.63	6.44	6.46	5.50	5.50
M±SD	***7.19± 1.01***	***7.35± 1.16***	***6.65± 0.23***	***6.61± 0.18***	***5.92± 0.67***	***5.58± 1.08***	***6.87± 0.84***	***6.83± 0.51***	***6.49± 0.25***	***6.53± 0.24***	***6.00± 0.52***	***5.75± 0.75***
P value	***<0.001***	***<0.001***	***<0.001***	***0.01***	*0.32*	*0.09*	***<0.001***	***<0.001***	***<0.001***	*0.27*	*0.25*	*0.25*

Table 2.4. Intraclass correlation coefficient (ICC) showing, for each study group, the absolute agreement between cone spacing metrics in two different sampling areas at two retinal locations.

Sampling area	**64 µm x 64 µm**		**204 µm x 204 µm**	
Retinal eccentricity	1.5 degrees	2.5 degrees	1.5 degrees	2.5 degrees
Healthy subjects				
ICC between S_{cc} and LCS*	**0.80**	**0.80**	**0.93**	**0.93**
ICC between S_{cc} and DRPD	0.33	0.26	0.24	0.44
ICC between LCS and DRPD	0.37	0.11	0.25	0.25
Retinal diseases				
ICC between S_{cc} and LCS	0.08	0.23	0.51	0.29
ICC between S_{cc} and DRPD	0.05	0.47	0.36	0.14
ICC between LCS and DRPD	0.27	0.26	0.36	0.25

In healthy subjects, the correlation between S_{cc} and LCS was high over both sampling areas (R^2=0.75, P<0.001; and R^2=0.88, P<0.001, over 64x64 µm and 204x24 µm respectively) (Figure 2.3). In patients with retinal diseases, the correlation between S_{cc} and LCS was poor over both sampling areas (R^2=0.018, P=0.53; and R^2=0.25, P=0.014, respectively).

The 95% LoA was slightly influenced by window size; the agreement between S_{cc} and LCS values over 204x204 µm areas was greater than 64x64 µm areas (Figure 2.3). This was associated with the greater percentage of 6*n* Voronois in patients with retinal diseases over a 204x204 µm sampling window.

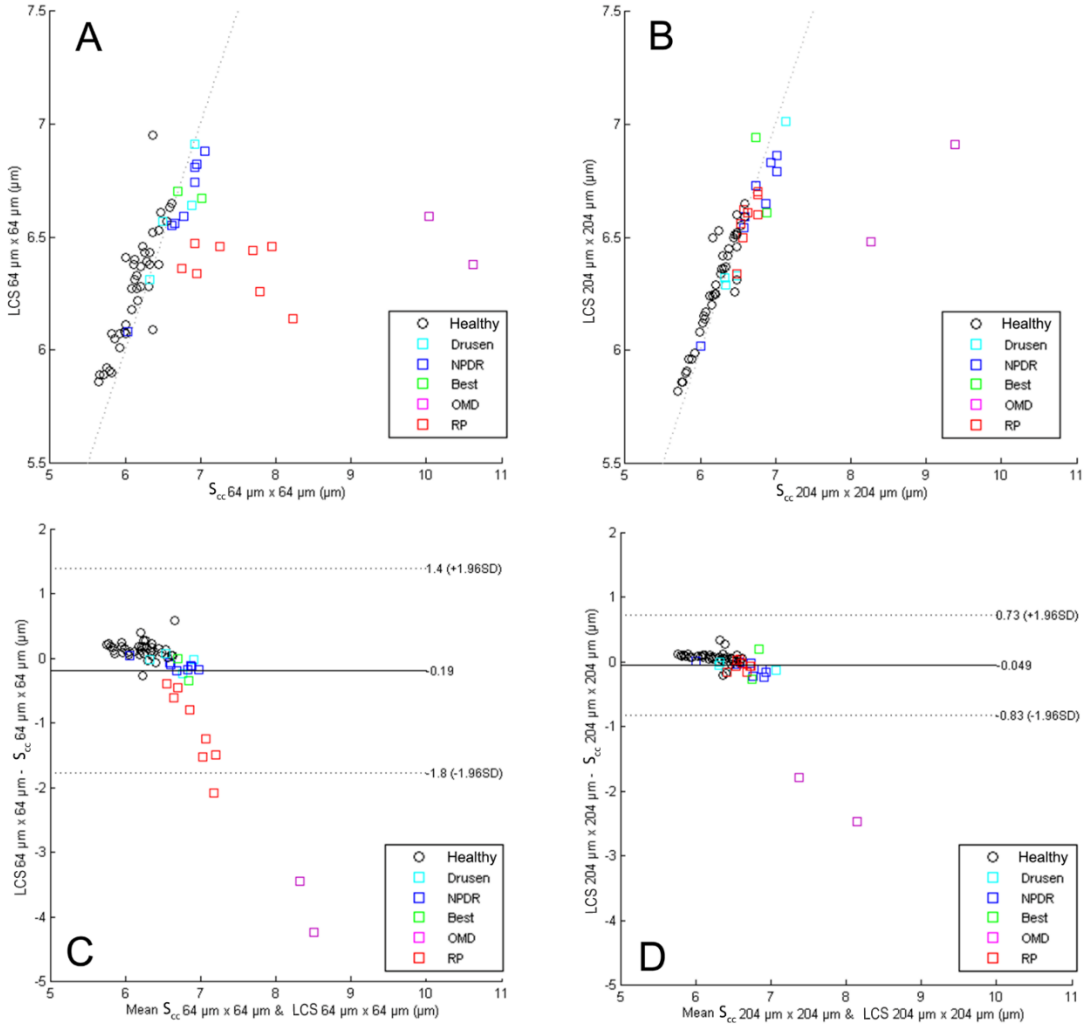

Figure 2.3 – A) Correlation between local cone spacing (LCS) and center-to-center spacing (S_{cc}) in 64x64 µm sampling areas. Data were aggregated from 1.5 degrees and 2.5 degrees retinal eccentricities. In healthy subjects, the correlation between LCS and S_{cc} was high (R^2=0.75, y=0.846x+1.082, P<0.001); almost all values (85%) were on the bisector (y=x, R^2=1). In patients with retinal diseases, the correlation between LCS and S_{cc} was very low (R^2=0.018, y=-0.028x+6.733, P=0.53); the patients with advanced stages of inherited retinal dystrophies (OMD and RP) and diffuse loss of cone reflectivity (≥30%) primarily contributed to the decreased correlation between this pair of spacing metrics. B) Correlation between LCS and S_{cc} in 204x204 µm sampling areas. In healthy subjects, the correlation was high (R^2=0.89, y=0.859x+0.946, P<0.001); 95% of the LCS and S_{cc} values were on the bisector. In patients with retinal diseases, correlation between LCS and S_{cc} was low (R^2=0.25, y=0.171x+5.433, P=0.01). C and D) Bland-Altman plots of S_{cc} and LCS values calculated over 64x64 µm and 204x204 µm sampling areas respectively. Although the agreement between this pair of spacing metrics was high in the 64x64 µm area, the use of greater sampling areas further increased agreement between metrics. The symbols are described in the plot.

2.3.2.2 Influence of the sampling area on Scc

The S_{cc} values calculated over sampling areas of different sizes showed high correlation both in healthy subjects (R^2=0.84, P<0.001) and patients with retinal diseases (R^2=0.66, P<0.001). On the other hand, the distribution of data points in the Bland-Altman plot showed that agreement was poor for S_{cc} values estimated from cone mosaics with more than 30% cone reflectivity loss (Figure 2.4).

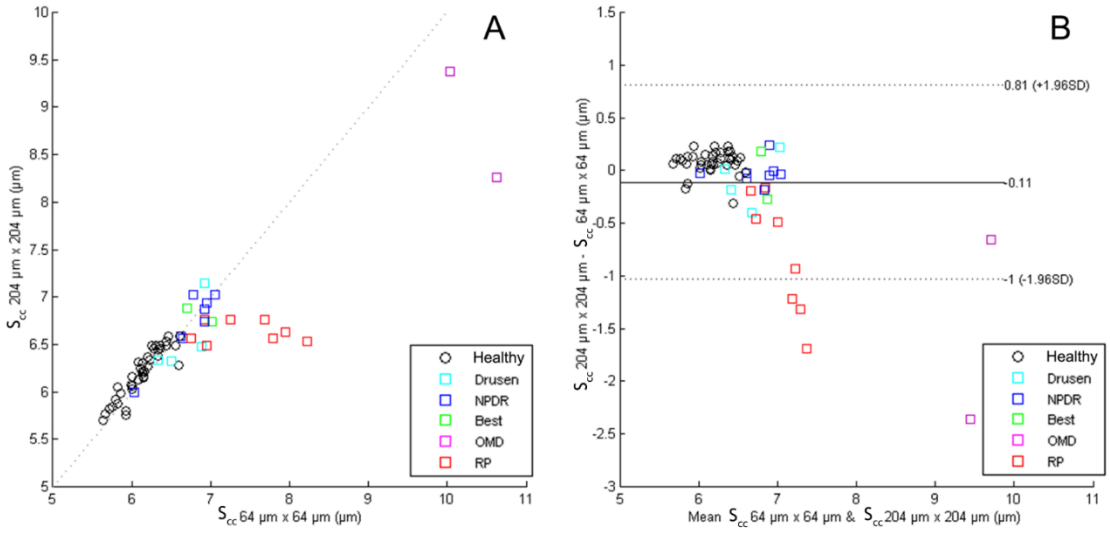

Figure 2.4 – A) Correlation between S_{cc} values calculated in the two sampling areas of 64x64 µm and 204x204 µm. In healthy subjects, the correlation was high (R^2=0.84, y=0.924x+0.541, P<0.001), with 85% of S_{cc} values that were on the bisector. In patients with retinal diseases, the correlation was moderate (R^2=0.67, y=0.517x+3.088, P<0.001); the patients with advanced stages of inherited retinal dystrophies (OMD and RP) and diffuse loss of cone reflectivity (≥30%) contributed to decrease the overall correlation between S_{cc} values taken over sampling areas of different sizes. B) Bland-Altman plot of S_{cc} values. The outliers in the Bland-Altman plot are represented by three patients (OMD, RP1 and RP4; see table 3.1) that had the lowest cone density in the study population. Data were aggregated from 1.5 degrees and 2.5 degrees from the fovea. The symbols are described in the plot.

2.3.2.3 Influence of the sampling area on LCS

The correlation between LCS values of the two sampling areas was high in healthy subjects (R^2=0.76, P<0.001) and moderate in patients with retinal diseases (R^2=0.46, P<0.001) at both retinal eccentricities (Figure 2.5). The 95% LoA showed scattered values around the bias line that tended to increase as the average LCS value increased.

2.3.2.4 Influence of the sampling area on DRPD

The correlation of DRPD values between the two sampling areas was moderate in healthy subjects (R^2=0.59, y=0.659x+2.02, P<0.001) and low in patients with retinal diseases (R^2=0.34, y=0.419x+3.466, P=0.003) at both retinal eccentricities. Both the scatter plot and the Bland-Altman plot (not shown) did not evidence any difference in the distribution of data points between healthy subjects and patients with retinal diseases.

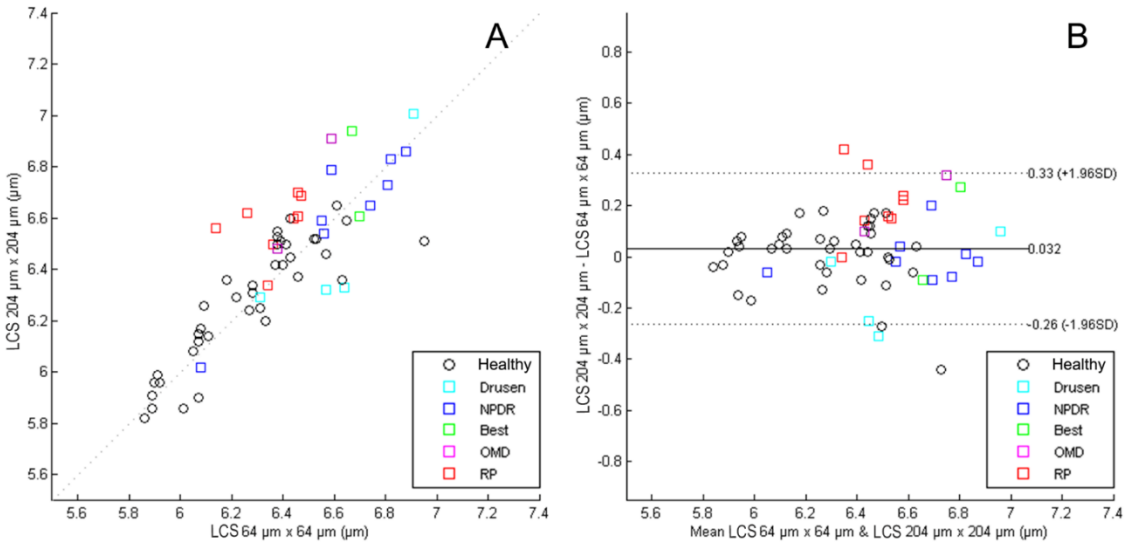

Figure 2.5 – A) Correlation of the LCS values calculated in the two sampling areas. In healthy subjects, the correlation between the LCS values was good (R^2=0.76, y=0.823x+1.116, P<0.001); on the other hand, it was moderate (R^2=0.46, y=0.715x+1.935, P<0.001) in patients with retinal diseases. B) Bland-Altman plot of the LCS values. Agreement between the LCS values calculated over sampling areas of different sizes was primarily decreased by patients with retinal diseases (i.e., for increasing values of LCS). Data were aggregated from 1.5 degrees and 2.5 degrees from the fovea. The symbols are described in the plot.

2.4 Discussion

We evaluated the agreement between three metrics currently used to describe the distribution of distances between cones in AO images of the cone mosaic. A group of healthy subjects and a group of patients with different retinal diseases and variable loss of cone reflectivity (from 2% to 65% with respect to healthy photoreceptor mosaic) were included in the study in order to understand if center-to-center spacing (S_{cc}), local cone spacing (LCS) and density recovery profile distance (DRPD), which have been calculated over sampling areas of different size, could be used interchangeably in clinical studies.

Both S_{cc} and LCS were able to discriminate between healthy subjects and patients with retinal diseases; on the other hand, DRPD did not reliably detect any abnormality in the distribution of distances in the study population. This is related to the fact that this metric is calculated from the shape of the DRP, which remains unchanged even for large undersampling (only the vertical scale, i.e., cone density, is influenced by cell loss) [39].

Previously, Cooper et al. [34] have shown - in simulated AOSLO images of the cone mosaic - that the DRPD was remarkably insensitive to undersampling of cone coordinates, being unable to classify as pathological mosaics with up to 60% loss of cone reflectivity. In the same study [34], the authors have found that NND was also insensitive to undersampling

(up to 50%). Therefore, the use of single spatial metrics based on DRPD or NND would not be clinically valuable to accurately discriminate between healthy and pathological photoreceptor mosaics. In order to overcome this major limit of NND in evaluating the distribution of cell distances in a human retinal cone mosaic, we have previously developed the LCS metric [44]. In this study, the S_{cc} and LCS were highly correlated and could be used interchangeably without incurring any methodological error until 20-25% of the cones in the given mosaic have been lost (e.g., cases with hard drusen and NPDR in this study). However, both correlation and agreement between this pair of spacing metrics dropped when cell reflectivity loss was ≥30%, primarily when comparison was made in 64x64 μm sampling areas (e.g., cases with inherited retinal dystrophies). In this study, cases with retinal diseases had significantly fewer six-sided Voronois than healthy cone mosaics, as expected. Since lattice quality diminishes with disease progression (as well as with retinal eccentricity even in healthy subjects) [34,38,44]. The S_{cc}, which provides a single-point estimate without a measure of variation and assumes an ordered lattice, is more prone to overestimating the integrity of the cone mosaic in retinal diseases than LCS. On the other hand, LCS alone may lose the sensitivity to detect small deviations from normal (<20% undersampling, as for example in hard drusen and NPDR cases in this study). Since the methodology of calculating LCS also indirectly provides estimates of both the standard deviation and mean of the distances between cells, the use of their ratio, previously termed Linear Dispersion index [44], has been shown to achieve enough sensitivity to evaluate the averaged distribution of cell distances across the parafovea in controlled clinical study.

The influence of the sampling window size was relevant for the analysis of intercell distance in AO images of the cone mosaic, possibly because photoreceptor loss is variable across areas of the retinal mosaic as well as among retinal diseases. Overall, the choice of the window size should avoid poor sampling. The use of smaller sampling windows, such as the conventional 64x64 μm area, allows for a local analysis of the integrity of the cone mosaic, while the use of larger areas, such as 204x204 μm, may lead to overestimating the integrity of the retinal mosaic, probably because of the presence of healthy domains of the cone mosaic in the area of analysis. As shown in figures 3.4 and 3.5, the use of smaller sampling areas would be preferable for tracking disease progression when using S_{cc} and LCS (and possibly NND). If data analysis were carried out over large sampling areas, the complementary use of more than one metric to describe the spatial arrangement of the cones would be preferable. We have already shown that the pathological decrease of cone density in adult subjects, even when density falls within normal limits, induces abnormal changes in the arrangement of the cones [44]; therefore, the complementary use of regularity indices

based on Voronoi analysis together with spacing and density metrics is very helpful to detect small deviations from normal cone mosaic arrangement [44,51].

The spacing metrics examined in this work do not represent the full list of metrics for evaluating the distribution of cell distances of a retinal mosaic. Several other metrics have been generated from the point coordinates of cells or directly from the AO image of the cone mosaic, such as those based on analysis of the Fourier spectrum of the image [34,52-59].

Currently, the main limit of any metric describing the spatial position of the cones is related to the correct cell identification. As disease progresses, cell loss and disorder in cell spacing increases, which in turn decreases resolution by distorting the AO image of the cone mosaic. Accurate cone identification and segmentation is required in order to minimize methodological errors [1,30,31,33,34]. The present AO images were acquired at 1.5 degrees superior and 2.5 degrees temporal from the PRL and the results from the present work cannot be directly extended to different areas of the retina. In previous studies [31,37,60] the PRL was found to deviate, on average, 27±15 μm from the foveal center, and the displacement of the PRL to foveal center was not correlated to SEr or AxL. Co-registration of AO images with OCT cross-section images would be desirable in clinical studies in order to avoid variation in determination of eccentricity caused by compromised vision that may have the PRL away from the anatomic foveal center. It was also outside the scope of this work to determine the best spacing metric to be used in clinical studies. Overall, as cone density and packing arrangement of the cones deviate from normal expected values, S_{cc} is less reliable than LCS to determine the distribution of cell distances in the human photoreceptor mosaic. The complementary use of density, spacing and regularity metrics is valuable to increase the sensitivity of each descriptor for evaluating small deviations of the cone mosaic from the normal expected packing density arrangement [34,44,45,49,51].

The use of other AO imaging modalities, such as non confocal split-detector based AOSLO, would enhance the identification of cell loss over other confocal or non confocal techniques [1,61]. For this reason, we preferred using the term loss of cone reflectivity instead of cone loss. Comparing the results of cone metrics calculated on images of the same mosaic collected by different AO imaging modalities would be valuable to understand differences between instruments.

In conclusion, the sampling window size and the method used for evaluating the distribution of cell distances in AO images of the human retinal cone mosaic should be considered when comparing spacing metrics between clinical studies.

Chapter 3

Statistical analysis of second-order properties of cone mosaic

3.1 Introduction

In the retina, decrease in cone density or spatial deviation from normal non-random arrangement may cause deterioration in visual quality. Accordingly, there is increasing interest to understand if there is a "normal" spatial arrangement of photoreceptors and if exists any correlation between photoreceptors on local, intermediate and long length scales. Understanding how the photoreceptors are packed may provide an indicator to detect retinal pathologies early in their onset in patients. In addition, this indicator could be valuable for monitoring *in vivo* the spatial distribution of photoreceptors over time and for monitoring the efficacy of novel therapies to slow down or halt photoreceptor loss at cellular level.

Currently, local spatial statistics, such as density, number of neighboring points and spacing metrics (see Chapter 2, par. 2.3.2), are based on the 2D distribution of the cones, provide global information about the spacing regularity of the cones in the given mosaic. Another systematic way to obtain this statistical information is to construct Voronoi graph associated with the spatial distribution of the cones. Each cone, identified by its geometrical centroid, corresponds to a Voronoi tile that is color coded with respect to their cones neighbors. In healthy photoreceptors mosaic, the hexagonal arrangement is predominant and it is usually analyzed by evaluating the percentage of six-neighbours cells or the area they occupy over the other cells.

Overall, all the currently used statistical approached provide useful local structural information on the photoreceptor mosaic but they lack to capture the salient mosaic features of spatial correlation between photoreceptors: how are they distributed? It is not straightforward to understand whether a spatial order exists and how we can quantify it.

On the other hand, techniques from the theory of heterogeneous media were used to characterize spatially optical images of the distribution of the cell nuclei, i.e. in brain tumors [62-65]. By identifying the geometrical centroids of the cell, a spatial distribution of cell can be modeled as a distribution of points. Point distributions are models used for many-particle systems in various branches of modern science, the aim of this work is to investigate novel classes of spatial and statistical microstructural descriptors, which arise in the theory of statistical mechanics and particle packing theory heterogeneous and condensed matter, such as liquid crystal, and employ them to characterize the spatial distribution of retinal photoreceptors. These models allow to study the spatial correlation of the points on short, intermediate and large scales, to investigate the mechanisms of the arrangement of a point distribution.

In general, models with various degrees of spatial correlations can be generated: a Poisson distribution is generated by randomly placing a prescribed number of points in a domain with fix volume, regardless the positions of existing points, it is an example of *Complete Spatial Randomness* (CSR); in a random sequential addition (RSA) distribution, no disk can overlap any other disks (i.e., the inhibition distance between any two disk centers must not be smaller than the diameter of the disks). Therefore, the points from a Poisson distribution are completely uncorrelated to each other, while a RSA distribution presents spatial correlations between the centers and respects the non-overlapping property of the real cell systems.

Here we used statistical second order descriptors to characterize the spatial distributions of photoreceptors in real and simulated images. These spatial descriptors include the pair correlation function $g_2(r)$, the structure factor s(k) and various nearest neighbor second order statistics (G(r), K(r) and L(r)), to quantify the reciprocal influence of the cells at a variable distance r.

We generated simulated pattern points with the Poisson distribution, that is often used in literature as reference system but is totally uncorrelated, and with the RSA distribution that is a more realistic simulation, thanks to the inhibition distance between points, like in real cell mosaic.

By comparing the statistics of the cone distributions to the reference systems, Poisson and RSA distribution and by directly comparing appropriately scaled (respect the intensity) distributions of normal and diseased cone mosaic (i.e., cone mosaic of patients affected from non proliferative diabetic retinopathy (NPDR) and inherited retinal disease (IRD)), we found that salient structural features related to different short and long arrangement of the cone mosaics, in healthy and diseased subjects, are captured very well by these correlation functions. Our results showed that the normal cone mosaic is more densely packed than diseased cone mosaic, holds stronger short-range correlations, and the distributions of cone photoreceptors in all study groups present different long-range spatial correlations. The difference between the spatial statistics of the three study groups suggests that different arrangement models can be developed to characterize the cone mosaic in normal eyes and eyes with retinal diseases, and that also in case of disease the rearrangement of the cone photoreceptors is not random but reflects a complex system, as in the healthy retina.

3.2 Methods

All research procedures described in this work adhered to the tenets of the Declaration of Helsinki. The protocol was approved by the independent local ethical committee and all subjects recruited gave written informed consent after a full explanation of the procedure. Inclusion criteria were age >18 years old, no previous eye surgery, eye inflammation, glaucoma or cataract. Subjects recruited for the study received a complete eye examination, including non-contact ocular biometry using the *IOL Master* (Carl Zeiss Meditec Inc, Jena, Germany).

3.2.1 Human subjects

Thirty-three healthy volunteers (age 33± 6 years old; gender: 20 F and 13 M), and ten patients with a diagnosis of acquired (n=6, age 48±9 years old; gender: 3 F and 3 M) or inherited (n=4, age 37±16 years old; gender: 2 F and 2 M) retinal diseases were recruited in this study. The latter participants included subjects with a diagnosis of non proliferative diabetic retinopathy (NPDR; n=6), according to the ETDRS severity scale [43,44], called in the text NPDR group, and of retinitis pigmentosa (RP; n=2; USH2A gene mutation), Best macular dystrophy (Best; n=1; BEST 1 gene mutation) and occult macular dystrophy (OMD; n=1; RP1L1 gene mutation) [45], called in the text IRD group.
These participants were enrolled in this study to have a dataset of AO images of the cone mosaic with increasing amount of cell loss and variable abnormalities in the packing arrangement of the cones.

3.2.2 Image acquisition and processing: Real data

The flood-illuminated AO retinal camera (*rtx1*, Imagine Eyes, France) was used to collect images of the cone mosaic on 33 healthy subjects and 10 subjects with various retinal diseases. The imaging session was conducted as described in Chap. 2 par. 2.2.2. In this study, a sampling area of 240x240 μm size was cropped from each final image at 2.0 degrees temporal from the fovea center, identified by using the corresponding optical coherence tomography (OCT) foveal images of each subject (Figure 3.1).

Image cone labelling was automatically performed using an enhanced version of the algorithm implemented with the image processing toolbox in Matlab (The Mathworks Inc,

Natick MA, USA) [30,31,43,44,48]. Cones were identified independently in each sampling window. The cone identification algorithm's performance was verified by three expert investigators, who reviewed each sampling area and manually identified cones that they agreed to be missed or selected in error by the algorithm. This procedure ensured that the number of excluded cones was minimised. A buffer zone was created in each sampling window in order to minimize the *boundary effect* for packing geometry metrics [30,31]. The *x*,*y* coordinates of the cones in each sampling window were stored in a text array, in this way we mapped the distributions of cone photoreceptors into point distributions, and then used to calculate the spatial statistics.

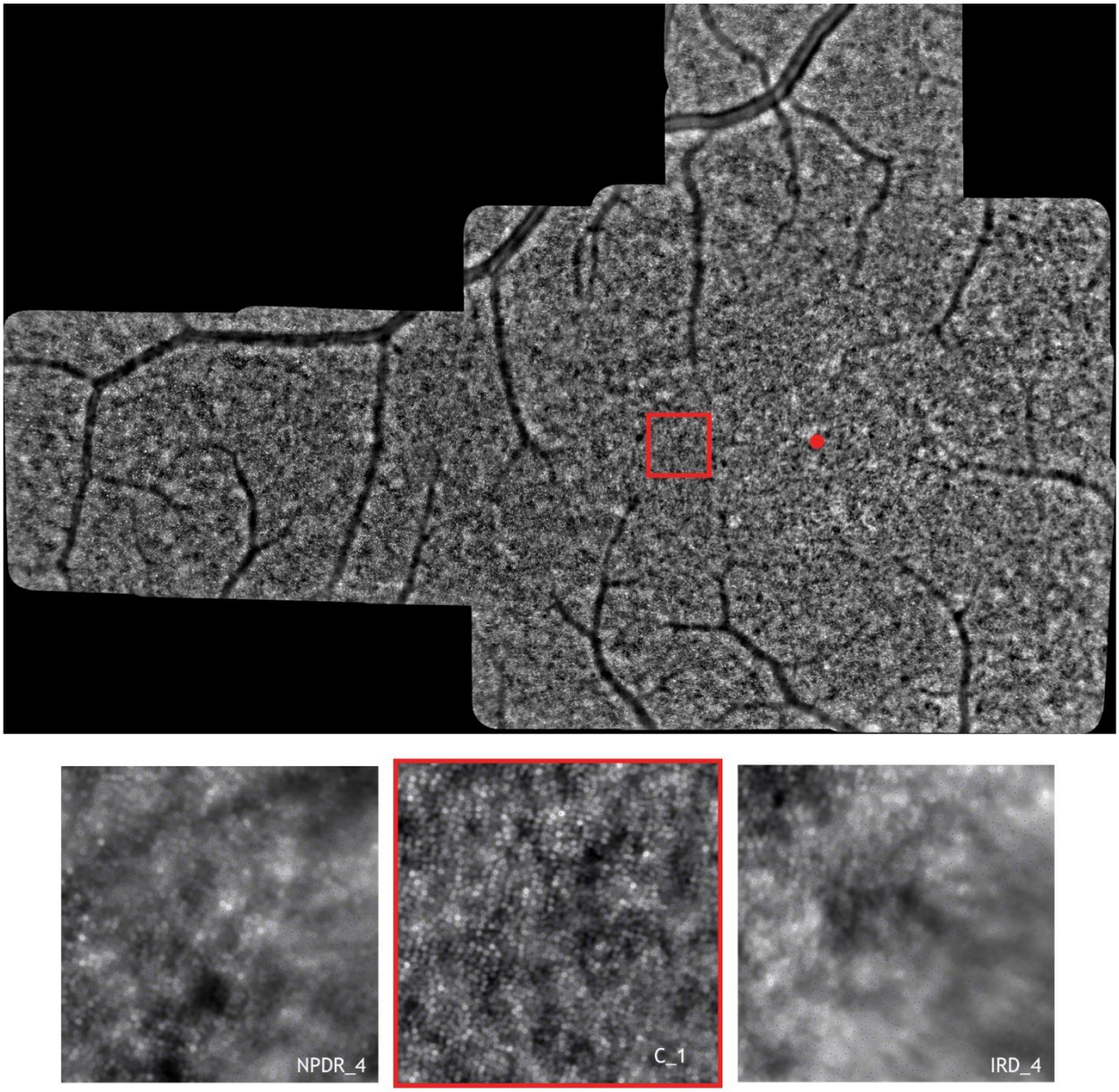

Figure 3.1. Up, AO montage of the photoreceptor mosaic in a healthy subject (C_1). The red dot shows the foveal center and the red square the sample area (240x240 µm). Down, cropped AO images with cone centroids in three representative cases. On the left, the image shows the mosaic appearance from a subject affected by NPDR, in the center the mosaic of a healthy subject and on the right, the retinal mosaic in a subject with Best macular dystrophy (IRD group).

3.2.3 Generation of Simulated data

As reference systems, we created two dataset of simulated pattern points (Figure 3.2). The customized algorithm in Matlab (The Mathworks Inc, Natick MA, USA) generated 50 cone densities from a normal distribution of mean and standard deviation of the cone density in Control group. For each one of these values, a homogeneous 2-D Poisson process of data points, uniformly distributed over the study region, and a random sequential addition (RSA) distribution with inhibition distance between any two centroids of 5 pixels, were built. As for the real data, the *x,y* coordinates of the points in each sampling window were then stored in a text array and used for subsequent analysis.

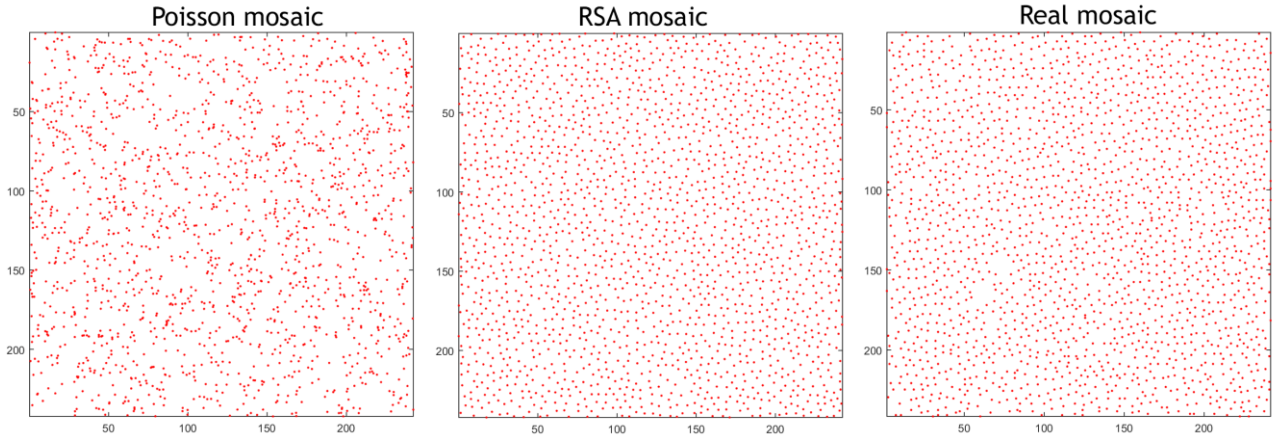

Figure 3.2. Examples of the Poisson, RSA and real mosaic after digitalization of the cone controid coordinates.

3.2.4 Spatial statistics

Spatial statistics concerns with statistical methods, which explore the spatial arrangement of points for discovering their spatial correlations or in general for inferring their overall behavior. Typically, data can fall into three categories: point patterns, geostatistical data and lattice data. In order to investigate the cone photoreceptor mosaic arrangement, methods that infer information from point patterns arrangement were evaluated.

Spatial point patterns are data made up of the location of *point events*. We investigated if their relative locations represent significant point patterns, i.e., whether such patterns are clustered or present some regularity or if they hold some specific spatial statistical point distribution. Moreover, the point-pattern data can be associated to an *attribute* of the spatial

events: i.e., the cone reflectance. Each point location $\boldsymbol{s_i}$ is a vector containing the coordinates of i-th events, $s_i=[x_i,y_i]$, located in the sampling window R. Theoretically, the study region can assume any shape, but care must be taken about the *edge effects* that can occur with the statistics methods used. The edge effects are handled by leaving a specified safeguard area around the edge of the study region, but still within R.

First order property of the spatial point patterns is in terms of the number of events, in our case events are the cone photoreceptors, occurring in an arbitrary sub-region R. We can denote the number of events in a sub-region A as Y(A). The spatial process is then represented by random variables Y(A), with A contained in R.

After digitizing the coordinates of the centroids of the cone reflectance on sampling window, exploratory methods of data analysis can be applied to characterize the 2D point process of cone photoreceptors. The most basic information is an estimate of the intensity $\boldsymbol{\lambda}$ of the point process, i.e. the mean (= E = expected) number of points per unit reference area. If Y(A) is a motion-invariant point process, in our case events are the cone photoreceptors, then

$$\lambda = \frac{E(Y(A))}{|A|} \qquad (3.1)$$

The intensity is correlated with the *cone density* but is referenced to a sub-region of R, whereas the cone density is referenced to whole study region R.

In order to understand the second-order properties of a spatial point process, we need to look at the number of events in pairs of sub-regions R. The second-order property reflects the spatial dependence in the process, $\gamma(s_i,s_j)$.

For understanding the behavior of the spatial point arrangement, we can compare the experimental/observed spatial cone location with a common benchmark spatial model like as the *Complete Spatial Randomness* (CSR). Events follow a homogeneous Poisson process over the study region. The definition is given by:

1. The intensity does not vary over the region. Thus, Y(A) follows a Poisson distribution with mean λA, where A is the area of A and λ is constant;
2. There are no interactions between events. This means that, for a given n, representing the total number of events in R, the events are uniformly and independently distributed over the region of interest.

In a CSR process, each event has the same probability of occurring at any location in R, and events are neither inhibit nor attract each other. To look for the presence of clusters and/or

regular spatial patterns, we study if the spatial patterns are statistically like a CSR process or departure from it.
In the following, methods used for estimating the first-order and second-order properties of the point-process were presented.

3.2.4.1 Intensity estimation

One methodology to summarize the events in a spatial point pattern is to divide the region of interest into sub-regions of equal size, which are termed quadrants, and to count the number of events falling in each sub-region. Then the intensity is estimated by dividing the number of events occurred in each sub-region with the sub-region area (Eq. 3.1).
Another method to estimate the intensity is the Kernel Estimation, which results are smoother than the quadrant method. The estimation of the intensity is given by:

$$\lambda_h = \frac{1}{\delta_h(s)} \sum_{i=1}^{n} \frac{1}{h^2} k\left(\frac{s-s_i}{h}\right) \qquad (3.2)$$

where k is the kernel function, h is the bandwidth and δ_h is the edge correction factor. An overly large h provides an estimate that is very smooth, hiding variation in the intensity; whereas a small bandwidth might indicate more variation than that are real, making it harder to see the overall pattern in the intensity. The kernel function we have implemented is the quartic kernel:

$$\lambda_h = \sum_{d_i \le h} \frac{3}{\pi h^2}\left(1 - \frac{d_i^2}{h^2}\right)^2 \qquad (3.3)$$

Where d_i is the distance between pairs of events locations and the correction for edge effects is not included.
We investigated the second-order properties of the point-process by studying the relationship of distance between events in the region of interest R and comparing their spatial distribution along distance to a random spatial point, Poisson, and to a random sequential addition, RSA, process. While the intensity is a single quantity, second-order functions provide a series of values as a function of the interpoint distance r. Their functional values indicate which kind of interaction between points prevails at a certain distance. This interaction may consist in attraction (clustering) or repulsion, or otherwise there may be no interactive effects between the points at all at a certain distance.

3.2.4.2 Nearest Neighbour Distance Function G

The nearest neighbour distance distribution function (also called the "event-to-event" or "inter-event" distribution) of a point process Y is the cumulative distribution function *G(r)* of the distance from a typical random point of Y to the nearest other point of Y.

An estimate of *G(r)* derived from a spatial point pattern dataset can be used in exploratory data analysis and formal inference about the pattern [66-68]. In exploratory analysis, the estimate of *G(r)* is a useful statistic summarizing one aspect of the "clustering" of points. For inferential purpose, the estimate of *G(r)* is usually compared to the true value of *G(r)* for a completely spatial random point process (i.e., CSR). Deviations between the observed and CSR theoretical *G(r)* curves may suggest spatial clustering or spatial regularity. *G(r)* measures the fraction of nearest-neighboring distances that are less than or equal to *r*:

$$G(r) = \frac{1}{n}\sum_{i=1}^{n} I(r_i \leq r) \qquad (3.4)$$

where r_i is the distance of events *i-th* to its nearest-neighbor and *n* are the total number of events in the study region, and *I* is an indicator function which assumes value of 1 if $r_i \leq r$ otherwise it is zero. Since *G(r)* is a cumulative probability, the range of *G(r)* is [0,1]. Hence, *G(r)* is normally evaluated over a range from 0 to some value *w* such that *G(r) = 1*.

3.2.4.3 K and L Functions

The empirical cumulative distribution function *G(r)* uses distances to the nearest neighbor, so it considers only the behavior of point patterns at the smallest scales. It would be useful to have an insight about the pattern at several scales: we can use an estimate of the *K-function*, which is related to the second order-properties of an isotropic process.

The definition is:

$$K(r) = \frac{A}{n^2}\sum_{i=1}^{n}\sum_{j\neq i}\frac{I(d_{ij}\leq r)}{\delta_{ij}} \qquad (3.5)$$

where d_{ij} is the distance between the i-th and j-th events and *I* is an indicator function that takes on the value of 1 if $d_{ij} \leq r$ and zero otherwise. The δ_{ij} is a correction factor for the edge effects. The *K(r)* function is the cumulative version of the Density Recovery Profile (DRP).

The advantage of the *K(r)* function is that it is not necessary to specify a bin width, and so we are not troubled by setting large bin widths when the number of cell bodies is low.

The estimated *K(r)* function can be also compared with a CSR spatial point process. The theoretical *K(r)* function for CSR is known and equal to $K(r) = \pi r^2$. An initial curve segment with $K(r) = 0$ indicates that the interpoint distance does not attain values below a certain minimum. In the case of biological structures such as cells, cell nuclei or capillaries, this behavior may simply result from their physical size, if no overlapping is possible. Such curve segments may hence be interpreted as a sign of a hard-core property. The lowest r-value for which the sample *K(r)* function reaches a positive value, r_0, may be considered as an estimate of the hard-core distance (see Table 4.1).

If the observed process exhibits regularity for a given value w, then we expect that the estimated *K(r)* function will be less than πr^2, alternatively if the spatial pattern presents a clustering behavior $K(r) \geq \pi r^2$.

Another approach, based on this assumption, is to define a characteristic length function, named *L(r)* function:

$$L(r) = \sqrt{\frac{K(r)}{\pi}} - r \qquad (3.6)$$

Peaks of positive value in a plot of *L(r)* vs *r* would correspond to clustering, with troughs of negative values indicating regularity for the corresponding *r*.

The *pair correlation function*, $g_2(r)$, (also known as *radial distribution function*, whose information is similar to that provided by an autocorrelogram) and the *structure factor*, s(k), may provide relevant information about short and long range spatial correlations order of retinal photoreceptors respectively [62].

3.2.4.4 Pair correlation function $g_2(r)$ and Structure factor: s(k)

Assuming again that the photoreceptor mosaic is a statistically homogeneous and isotropic system, $g_2(r)$ is a measure of the probability of finding a particle at distance *r* away from a given cone photoreceptor. The pair correlation function $g_2(r)$ may be obtained after differentiation and normalization of *K(r)*:

$$g_2(r) = \frac{1}{2\pi r}\frac{dK(r)}{dr} \qquad (3.7)$$

In the case of a Poisson point process:

$$g_2^{Poi}(r) \equiv 1 \tag{3.8}$$

for all r (by insertion of $K(r)=\pi r^2$ into eq. (3.7)).

In general, the algorithm involves determining how many particles are within a distance *r* and *r+dr* from each cone. The $g_2(r)$ function should be used to characterize spatial correlation between pairs of cones on a relatively short scale length. Since two cones can never occupy the same space, the probability of finding two cones at the same place (i.e., r = 0) is zero, so that $g_2(r = 0) = 0$. At finite separations, the relative position of a given cone can be influenced by the other cones in the same mosaic, which leads to variation in probability of finding cones at certain distances away from a given cone. The way in which $g_2(r)$ assumes values greater than 0 holds information on the spatial correlation between cones at short range. Moreover, for higher values of *r*, $g_2(r)$ approaches its asymptotic value to unity, meaning that the probability to finding two cones at relative large distance is constant (i.e., there is uniform probability). Values of $g_2(r)$ below 1 indicate repulsion, value above 1 indicate clustering for point pairs of such a distance *r*. Hills and valleys above and below the constant value 1 indicate domains of *r*-values with tendencies of the points for aggregation and repulsion, respectively.

In the same way, the *structure factor*, which is defined for statistically homogeneous and isotropic systems as:

$$s(k) = 1 + \delta h(k) \tag{3.9}$$

where δ is cone density, $h(k)$ is the Fourier transform of the total correlation function $h(r) = g_2(r) - 1$ and *k* is the wavenumber of the reciprocal variable *r*, ($k=2\pi n/L$, with $n=1,2,3\ldots$ and *L* is the linear size of the system).

For non-ordered systems, the $s(k)$ value associated to small k reflects the long-range correlation in the mosaic in the real space. Therefore, small $s(k)$ behavior for small *k* values is related to the way $g_2(r)$ approaches its large *r* asymptotic value to unity. In other words, $s(k)$ for small *k* values reflects the degree to which there exists large-scale collective organizations in the spatial distributions of cones.

If the cones are not correlated on a long scale length, i.e., the position of the cones is not influenced by cones that are far away in the mosaic, the *structure factor* is equal to unity for

all values of *k*. If the spatial distribution of cones possesses long-range spatial correlations, variations in *s(k)* from unity should be observed for low *k* values.

3.2.5 Statistical methodology

Data were expressed as mean ± standard deviation. Statistics were performed using the SPSS software (version 17.1; SPSS Inc., Chicago, IL USA) and Matlab (version R2013a, The Mathworks Inc., Natick MA, USA). The 95% confidence intervals of the spatial function were computed by bootstrap methods with 1000 bootstrap samples for each *r*-value.
After Kruskal Wallis test, the differences between the spatial statistics at fixed *r* of the two patient groups, respect the control group, the RSA and Poisson simulations group were evaluated using the non-parametric Mann Whitney U test, while independent-samples t-test was performed to compare control with RSA and Poisson simulations, due to the multiple comparisons a Bonferroni correction was applied. A P-value < 0.05 was considered statistically significant.

3.2.6 Summary characteristics

In addition, to the local computation of confidence intervals and significance tests for fixed *r*, to summarize the course of the $g_2(r)$ by a single quantity, from each estimated function was extracted a statistic. By identification of the first maximum g_{max} and the next following minimum g_{min} with the corresponding *r* values r_{max} and r_{min} for each g-function, where $r_{min} > r_{max}$, the follow statistic was computed [69]:

$$M = \frac{g_{max} - g_{min}}{r_{min - r_{max}}} \tag{3.10}$$

The statistic *M* is related to the global degree of order in the spatial point pattern. Large values indicate a high degree of order and may be expected e.g. in the case of point patterns with an element of periodicity.

3.3 Results

The mean intensity and the mean cone density were 20% and 29% lower in NPDR than control eyes respectively (P<0.01); they were 75% and 50% lower in IRD than control eyes respectively (P<0.01). Data are summarized in Table 3.1.

The summarizing characteristics r_{max}, g_{max}, r_{min} and g_{min} were computed for all individual $g_2(r)$ functions. From these values, the statistic *M* was computed. The minimum interpoint distance r_0 was also recorded for each K(r) function. As showed in Table 3.1, there were no significant differences between the mean values of this parameters in the NPDR group compared to the control. On the contrary, there were high significant increase of mean g_{max}, r_{min} and g_{min}, in the IRD group. These finding corroborate that cones patterns of control and patient groups are spatially different, although the significant differences between control and NPDR patients were only in terms of intensity/density.

Table 3.1. Mean (±*SD*) summary characteristics in study participants over the sampling area at 2.0 degrees temporal from the fovea center.

Estimate	*Control group*		*NPDR group*		*IRD group*		*Level of significance Cont/NPDR*	*Level of significance Cont/IRD*
	$\bar{x}$	*SD*	$\bar{x}$	*SD*	$\bar{x}$	*SD*		
Density (ncones/mm^2)	28181	2057	21715	3241	14418	4246	0.001	0.001
Intensity λ	0.042	0.003	0.035	0.006	0.024	0.007	0.007	0.001
r_0 (μm)	3.39	0.45	3.33	0.33	3.00	0.40	N.S.	N.S.
r_{max} (μm)	5.04	0.58	5.33	0.83	5.60	0.92	N.S.	N.S.
g_{max} (μm)	1.43	0.08	1.44	0.11	1.59	0.14	N.S.	0.014
r_{min} (μm)	8.00	0.00	8.00	0.00	10.40	4.80	N.S.	0.004
g_{min} (μm)	0.90	0.06	0.98	0.08	1.20	0.15	N.S.	0.001
M	0.19	0.08	0.18	0.12	0.14	0.12	N.S.	N.S.

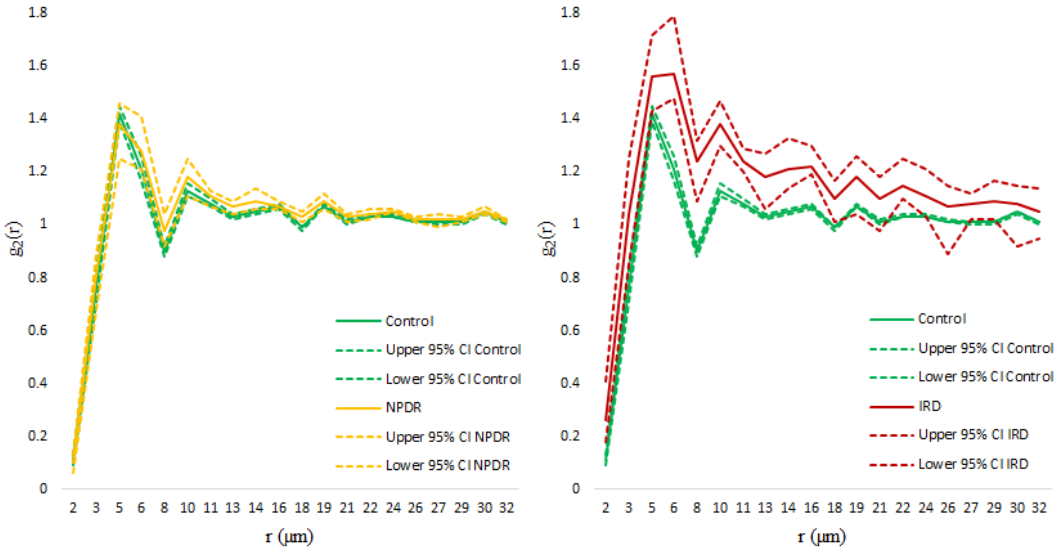

Figure 3.3. Example of the mean $g_2(r)$ with the 95% confidence intervals in the three real groups.

For the further analysis, the means of the spatial functions for each *r* in the study groups were estimated, and the 95% confidence intervals were computed by bootstrap method (1000 samples), see Figure 3.3 and Table 3.2-6.

At short range (*r*=1-15 µm; *k*=1-30), all the spatial functions showed significant difference ($P<0.05$) between the values in the control, NPDR and IRD groups in comparison with the Poisson simulation group at all the r values. At intermediate range, the mean spatial curves of control and NPDR groups approached the Poisson profile, while the IRD group was significantly different (Figure 3.4-8). The mean control spatial functions showed very similar profile with the RSA simulations; however, significant differences were found for G(r) in the range 3-6 µm, for the K(r) and $g_2(r)$ in almost all the *r* values, although the profile appeared equal by visual inspection, for the L(r) in the range 1-12 µm and for the s(k) under wavenumber k=30. The NPDR group showed similar results, while for the curves relative to the IRD group we found significant differences ($P<0.05$) at all the fixed *r*.

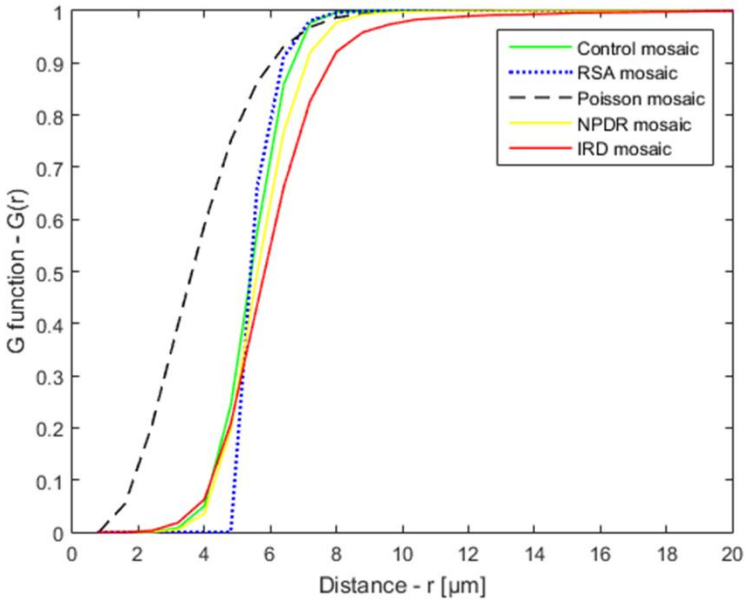

Figure 3.4. Mean G(r) function in all the real and simulated study groups. In the range r=2-5 µm, the inhibition distance, the mean G(r) of real groups are very close and high different respect Poisson and RSA simulated mean curves. The Poisson distribution theoretically has no inhibition distance, while the RSA distribution presents an inhibition distance exactly about 5 µm. The real curves are placed between these two cases: presenting much regularity respect a Poisson process, but less than the very regular RSA process. From 6 to 10 µm, all the curves approach the Poisson profile but with different slope: RSA and control mean curves are overlapped, and NPDR and IRD show a delay to reach the unity, bigger for the IRD group. So, in the second part the curves reach the unity with different velocity, proportional to cone density, loss of cones may determine this a minor tendency to aggregation in the photoreceptor cells.

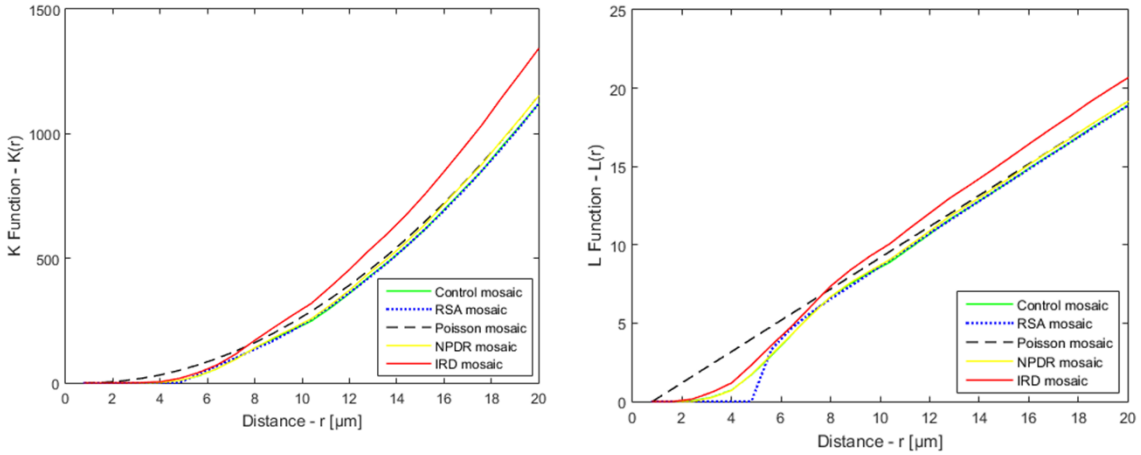

Figure 3.5. Mean K(r) and L(r) functions in all the real and simulated study groups. In the first part of the profiles, below 8 µm, all the groups show regularity respect the Poisson profile. In the L(r) graph the RSA and real mean curves appear not overlapped, with a higher regulatory for the RSA points pattern, followed by NPDR and control, overlapped, and finally IRD. In the second part of the profiles, over 8 µm, the RSA, control and NPDR mean curves approach the Poisson profile, while the IRD mean K(r) and L(r) functions show a clustering feature.

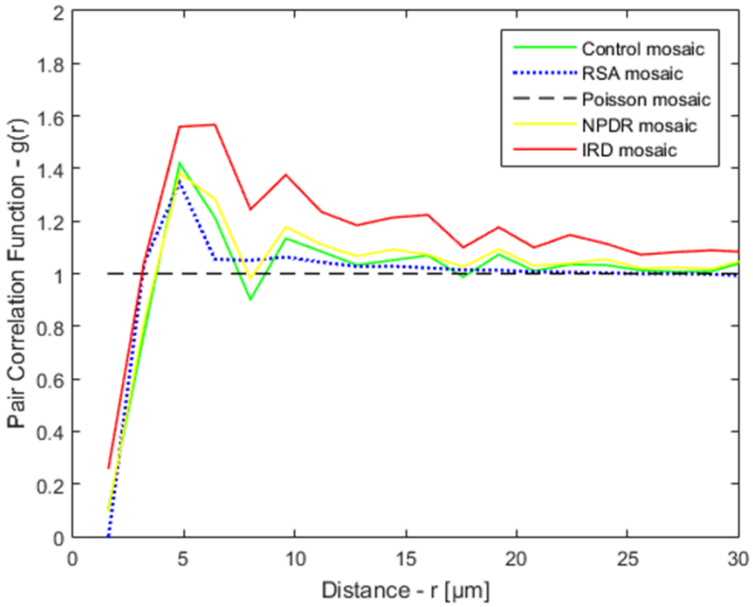

Figure 3.6. Mean $g_2(r)$ function in all the real and simulated study groups. In the range r=0-3 µm all the mean curves show repulsion tendency between cells, due to the inhibition distance. At r= 5 µm, the tendency to aggregation of the photoreceptor cells are max with a first positive peak, then all the mean functions approach the unity with the characteristic trend with hills and valley, except for the IRD $g_2(r)$ profile that remains far from the unity. This great tendency for aggregation of the IRD pattern points is a sign of high clustering.

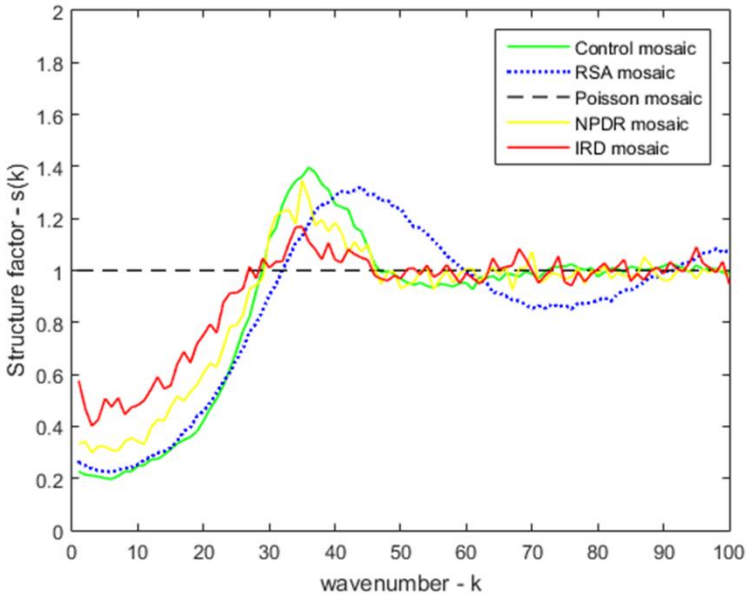

Figure 3.7. Mean s(k) function in all the real and simulated study groups. In the range k=0-30 s(k) gives information about the long range organization of the pattern points. In this specific range we observe that all the mean s(k) profiles deviate from the Poisson, so all the mosaic present a non random arrangement at long range. Control and RSA curves are almost overlapped, while the NPDR and IRD are well distinguishable. Furthermore, it seems that more the mosaic is packed densely, more is the distance from the Poisson plot, so high cone density leads a greater communication between cells at long range distance.

In the real study groups (Table 3.2-6), significant differences in the range r=6-9 μm were found for the mean G(r) function ($P<0.01$), in the range r=10-20 μm were found for the mean K(r) and L(r) functions ($P<0.05$) and in the range k=1-20 for the mean s(k) ($P<0.05$) between the Control and the NPDR group, no differences in the two $g_2(r)$ profiles. Finally, the comparison between the control and the IRD groups' mean spatial functions showed significant differences in the range r=6-18 μm for the G(r) function ($P<0.01$), in the range r=4-20 μm for the K(r) function ($P<0.05$), in the range r=3-20 μm for the L(r) function ($P<0.05$), in the range r=3-16 μm for the $g_2(r)$ function ($P<0.05$) and for the structure factor s(k) in the range k=1-25, as shown in Table 3.2-6.

3.4 Discussion

In the present study, parametric and non parametric methods were used to compare mean values of five spatial functions (G(r), K(r), L(r), $g_2(r)$ and s(k)) in a dataset composed of the retinal cone mosaic of healthy subjects, patients with different severity of retinal diseases, and two simulated pattern points from a Poisson and a random sequential addition (RSA) distributions. The estimated spatial functions from these pattern points quantified regularity or clustering characteristics at short, intermediate (G(r), K(r), L(r), $g_2(r)$) and long range (s(k)). The G(r) function estimates the Nearest Neighbour Distance by describing as the probability of find two cells approaching the unity for the fixed r values. Comparing the K(r) and the L(r) functions profiles with those relative to a CSR model (or Poisson in our case) is a method that can be used to quantify the regularity and clustering of the pattern points: domains of r values of these curves below the Poisson spatial function measures the regularity, while the values over the function measure clustering. Also, the pair correlation function $g_2(r)$ gives information about short range arrangement of cells: the hard-core effect leads to an initial segment with zero values, then hills and valleys above and below the unit indicate domains of r values with tendencies of the points for aggregation (clustering) and repulsion, respectively. Finally, short range of k values in the structure factor s(k), reflects the long range arrangement of the pattern points, in a CSR process the s(k) is constant equal to the unit, deviation from this value quantifies deviation from total uncorrelated pattern points.

Local approach with consecutive significance tests at fixed r/k-values was chosen, in order to investigate at which specific ranges of interaction the significant differences between the mean spatial function values in the study groups emerge. At short range (*r*=1-15 µm; *k*=1-30), the observed point processes were not compatible with simulation from Poisson point distribution. The property of non overlapping of the photoreceptor cells clearly characterized these pattern points as "hard-core" point processes. The other used simulation model, RSA, was generated starting from extracted data of the empirical images such as cone density and intercell distance, this leads to a more realistic simulated pattern point that showed in the results very similar profile respect those of the control group. Nevertheless, significant differences were found between RSA and Control, NPDR, IRD mean spatial functions at several *r* values: for G(r) function in the range 3-6 µm, 3-10 µm and 2-18 µm respectively; for K(r) function in the range 3-15 µm, 3-20 µm and 3-28 µm respectively; for L(r) and $g_2(r)$ at almost all the *r* values; and for s(k) factor in the range 25-70, 1-55 and 1-80 respectively. The RSA model appeared to have very high regularity respect to the control one, as a matter of fact, the mean L(r) curve of the RSA showed the bigger area below the Poisson mean curve, that is a measure of regularity. A solution to have a better simulated model may be to generate the pattern points with different inhibition distance, to mimic the variability present in real cone mosaic.

At short range, few differences at fixed r values were found between control and NPDR groups, the mean functions showed similar profiles, that signifies very regularity at short range and no clustering of these pattern points, as showed in the mean K(r) and L(r) functions that were below the Poisson mean curve for all the r values. The mean spatial functions relative to the IRD group showed a lot of significant differences respect control and simulated groups. This is the only group with high clustering tendency: in the mean K(r) and L(r) function the curves were over the Poisson profile starting from r=8 µm, the mean $g_2(r)$ is above 1 for all the r-values at short and intermediate range.

At long range, k=1-30, the mean s(k) factor of all the groups showed differences respect the Poisson mean curve: mean s(k) curves of Control and RSA groups were overlapped, while the NPDR and IRD groups demonstrate less difference in comparison with the Poisson pattern points. With decreasing in cone density (intensity), the long range spatial correlation appeared to decrease, indeed the mean s(k) relative to the IRD group was the nearest to the Poisson mean s(k).

The G(r), K(r), L(r), $g_2(r)$ and s(k) functions showed high sensitivity to discriminate between healthy and diseased retinal cone mosaics; the healthy retinal cones are more densely packed than pathologic retinal mosaics and possess stronger short and long range correlations. The

RSA, with some improvement to decrease the very high regularity for example by a variable inhibition distance, could be a good candidate to model real retinal photoreceptor mosaics. In addition, these spatial functions could be valuable for monitoring the spatial arrangement and distribution of photoreceptors over time in patients and for monitoring the efficacy of novel therapies to slow down or halt photoreceptor loss at cellular level.

Table 3.2. Mean (±SD), bootstrap bounds and P value for the G(r) function in the three real case groups.

r (μm)	$\overline{G}(r)$	*SD*	*Bootstrap bounds*		$\overline{G}(r)$	*SD*	*Bootstrap bounds*		$\overline{G}(r)$	*SD*	*Bootstrap bounds*		*Level of significance*	
Normal photoreceptor mosaic					*NPDR photoreceptor mosaic*				*IRD photoreceptor mosaic*				*Normal/NPDR*	*Normal/IRD*
1	0.00	0.00	0.00	0.00	0.00	0.00	0.00	0.00	0.00	0.00	0.00	0.00	N.S.	N.S.
2	0.00	0.00	0.00	0.00	0.00	0.00	0.00	0.00	0.00	0.00	0.00	0.00	N.S.	N.S.
3	0.01	0.01	0.01	0.01	0.00	0.00	0.00	0.01	0.02	0.02	0.01	0.03	N.S.	N.S.
4	0.05	0.03	0.04	0.06	0.04	0.02	0.02	0.05	0.06	0.03	0.04	0.10	N.S.	N.S.
5	0.24	0.08	0.21	0.27	0.20	0.06	0.15	0.23	0.21	0.06	0.18	0.27	N.S.	N.S.
6	0.86	0.08	0.83	0.88	0.77	0.09	0.70	0.83	0.66	0.08	0.57	0.72	0.018	0.003
7	0.98	0.02	0.97	0.98	0.92	0.04	0.89	0.95	0.83	0.08	0.71	0.88	0.002	0.001
8	1.00	0.00	1.00	1.00	0.98	0.02	0.96	0.99	0.92	0.06	0.83	0.95	P<0.001	P<0.001
9	1.00	0.00	1.00	1.00	0.99	0.01	0.98	1.00	0.96	0.04	0.90	0.98	P<0.001	P<0.001
10	1.00	0.00	1.00	1.00	1.00	0.00	1.00	1.00	0.98	0.02	0.95	0.99	N.S.	P<0.001
11	1.00	0.00	1.00	1.00	1.00	0.00	1.00	1.00	0.99	0.02	0.96	1.00	N.S.	P<0.001
12	1.00	0.00	1.00	1.00	1.00	0.00	1.00	1.00	0.99	0.01	0.97	1.00	N.S.	0.004
13	1.00	0.00	1.00	1.00	1.00	0.00	1.00	1.00	0.99	0.01	0.98	1.00	N.S.	0.004
14	1.00	0.00	1.00	1.00	1.00	0.00	1.00	1.00	0.99	0.01	0.98	1.00	N.S.	0.004
15	1.00	0.00	1.00	1.00	1.00	0.00	1.00	1.00	1.00	0.01	0.99	1.00	N.S.	0.004
16	1.00	0.00	1.00	1.00	1.00	0.00	1.00	1.00	1.00	0.01	0.99	1.00	N.S.	0.004
17	1.00	0.00	1.00	1.00	1.00	0.00	1.00	1.00	1.00	0.00	0.99	1.00	N.S.	0.004
18	1.00	0.00	1.00	1.00	1.00	0.00	1.00	1.00	1.00	0.00	0.99	1.00	N.S.	0.004
19	1.00	0.00	1.00	1.00	1.00	0.00	1.00	1.00	1.00	0.00	1.00	1.00	N.S.	N.S.
20	1.00	0.00	1.00	1.00	1.00	0.00	1.00	1.00	1.00	0.00	1.00	1.00	N.S.	N.S.

Table 3.3. Mean (±SD), bootstrap bounds and P value for the K(r) function in the three real case groups.

r (μm)	$\overline{K}(r)$	*SD*	*Bootstrap bounds*		$\overline{K}(r)$	*SD*	*Bootstrap bounds*		$\overline{K}(r)$	*SD*	*Bootstrap bounds*		*Level of significance*	
Normal photoreceptor mosaic					*NPDR photoreceptor mosaic*				*IRD photoreceptor mosaic*				*Normal/NPDR*	*Normal/IRD*
1	0	0	*0*	*0*	0	0	*0*	*0*	0	0	*0*	*0*	N.S.	N.S.
2	0	0	*0*	*0*	0	0	*0*	*0*	0	0	*0*	*0*	N.S.	N.S.
3	0	0	*0*	*0*	0	0	*0*	*0*	1	1	*1*	*2*	N.S.	N.S.
4	2	1	*2*	*2*	2	1	*1*	*2*	5	2	*3*	*7*	N.S.	0.003
5	9	3	*8*	*10*	10	2	*8*	*11*	17	6	*12*	*23*	N.S.	0.004
6	56	9	*53*	*59*	56	8	*48*	*61*	72	14	*60*	*83*	N.S.	0.013
7	96	7	*94*	*98*	95	9	*87*	*101*	116	16	*103*	*129*	N.S.	0.022
8	140	4	*139*	*142*	141	8	*134*	*145*	171	22	*155*	*194*	N.S.	0.045
9	178	3	*177*	*179*	181	7	*176*	*186*	222	27	*203*	*250*	N.S.	0.010
10	249	3	*248*	*250*	258	10	*254*	*269*	320	34	*292*	*347*	N.S.	0.001
11	301	6	*299*	*303*	313	13	*306*	*326*	386	42	*352*	*419*	N.S.	0.001
12	358	8	*356*	*361*	372	17	*362*	*388*	455	43	*419*	*490*	0.004	0.001
13	423	6	*421*	*425*	438	17	*428*	*455*	529	41	*495*	*563*	0.000	0.001
14	547	3	*545*	*548*	564	17	*556*	*584*	674	43	*638*	*710*	0.016	0.001
15	617	3	*616*	*618*	636	21	*626*	*660*	757	46	*720*	*794*	0.047	0.001
16	694	4	*693*	*696*	717	24	*705*	*745*	847	51	*806*	*887*	0.013	0.001
17	773	6	*771*	*775*	797	30	*783*	*832*	940	56	*896*	*996*	0.002	0.001
18	942	7	*940*	*945*	969	32	*953*	*1005*	1139	62	*1087*	*1200*	0.000	0.001
19	1030	6	*1028*	*1032*	1059	32	*1042*	*1096*	1239	66	*1187*	*1305*	0.000	0.001
20	1119	7	*1117*	*1121*	1151	36	*1133*	*1193*	1341	73	*1292*	*1414*	0.000	0.001

Table 3.4. Mean (±SD), bootstrap bounds and P value for the L(r) function in the three real case groups.

r (μm)	$\overline{L}(r)$	*SD*	*Bootstrap bounds*		$\overline{L}(r)$	*SD*	*Bootstrap bounds*		$\overline{L}(r)$	*SD*	*Bootstrap bounds*		*Level of significance*	
Normal photoreceptor mosaic					*NPDR photoreceptor mosaic*				*IRD photoreceptor mosaic*				*Normal/NPDR*	*Normal/IRD*
1	0.00	0.00	0.00	0.00	0.00	0.00	0.00	0.00	0.00	0.00	0.00	0.00	N.S.	N.S.
2	0.00	0.00	0.00	0.00	0.00	0.00	0.00	0.00	0.00	0.00	0.00	0.00	N.S.	N.S.
3	0.27	0.15	0.22	0.31	0.25	0.14	0.12	0.33	0.59	0.22	0.45	0.82	N.S.	0.003
4	0.73	0.22	0.65	0.80	0.70	0.20	0.57	0.85	1.18	0.28	1.01	1.46	N.S.	0.004
5	1.70	0.32	1.58	1.81	1.73	0.24	1.53	1.87	2.33	0.43	1.94	2.69	N.S.	0.012
6	4.22	0.33	4.09	4.32	4.23	0.32	3.94	4.40	4.76	0.46	4.32	5.14	N.S.	0.038
7	5.53	0.21	5.46	5.59	5.49	0.27	5.27	5.65	6.06	0.42	5.71	6.48	N.S.	0.011
8	6.68	0.09	6.65	6.71	6.69	0.19	6.50	6.79	7.36	0.48	7.02	7.86	N.S.	0.001
9	7.52	0.06	7.50	7.54	7.59	0.14	7.47	7.69	8.40	0.50	8.01	8.92	N.S.	0.001
10	8.90	0.05	8.88	8.91	9.06	0.16	8.98	9.26	10.08	0.53	9.64	10.55	P<0.001	0.001
11	9.79	0.10	9.75	9.82	9.97	0.20	9.87	10.21	11.07	0.60	10.58	11.63	0.015	0.001
12	10.68	0.12	10.64	10.72	10.87	0.24	10.74	11.12	12.02	0.57	11.51	12.49	0.041	0.001
13	11.61	0.09	11.58	11.64	11.81	0.23	11.67	12.01	12.97	0.50	12.49	13.33	0.015	0.001
14	13.19	0.04	13.17	13.20	13.40	0.21	13.30	13.65	14.64	0.47	14.17	15.03	P<0.001	0.001
15	14.01	0.03	14.00	14.02	14.22	0.23	14.12	14.50	15.52	0.47	15.09	15.90	P<0.001	0.001
16	14.87	0.05	14.85	14.88	15.10	0.25	14.98	15.40	16.42	0.50	16.02	16.80	P<0.001	0.001
17	15.68	0.06	15.66	15.70	15.93	0.29	15.79	16.28	17.29	0.51	16.81	17.67	P<0.001	0.001
18	17.32	0.06	17.30	17.34	17.56	0.29	17.42	17.92	19.04	0.52	18.60	19.50	0.001	0.001
19	18.11	0.05	18.09	18.13	18.35	0.28	18.22	18.70	19.85	0.52	19.44	20.32	P<0.001	0.001
20	18.87	0.06	18.85	18.89	19.14	0.30	18.99	19.49	20.65	0.56	20.28	21.22	P<0.001	0.001

Table 3.5. Mean (±SD), bootstrap bounds and P value for the pair correlation function $g_2(r)$ in the three real case groups.

r (μm)	$\bar{g}_2(r)$	*SD*	*Bootstrap bounds*		$\overline{g_2}(r)$	*SD*	*Bootstrap bounds*		$\overline{g_2}(r)$	*SD*	*Bootstrap bounds*		*Level of significance*	
Normal photoreceptor mosaic					*NPDR photoreceptor mosaic*				*IRD photoreceptor mosaic*				*Normal/NPDR*	*Normal/IRD*
2	0.11	0.06	0.09	0.13	0.10	0.05	0.06	0.13	0.26	0.13	0.18	0.41	N.S.	N.S.
3	0.77	0.18	0.71	0.83	0.81	0.14	0.68	0.89	1.04	0.23	0.85	1.25	N.S.	0.047
5	1.42	0.09	1.39	1.45	1.38	0.14	1.25	1.46	1.56	0.16	1.43	1.72	N.S.	0.002
6	1.21	0.14	1.17	1.26	1.28	0.13	1.21	1.41	1.57	0.16	1.48	1.79	N.S.	0.001
8	0.90	0.06	0.88	0.92	0.98	0.08	0.92	1.04	1.24	0.13	1.09	1.32	N.S.	0.001
10	1.13	0.08	1.11	1.16	1.18	0.09	1.11	1.25	1.38	0.10	1.30	1.47	N.S.	0.002
11	1.08	0.05	1.07	1.10	1.11	0.04	1.07	1.13	1.24	0.06	1.20	1.29	N.S.	0.019
13	1.03	0.03	1.02	1.04	1.07	0.03	1.04	1.09	1.18	0.12	1.06	1.27	0.028	0.002
14	1.05	0.03	1.04	1.06	1.09	0.05	1.06	1.14	1.21	0.12	1.14	1.33	N.S.	0.001
16	1.07	0.02	1.06	1.08	1.07	0.02	1.06	1.09	1.22	0.05	1.19	1.30	N.S.	N.S.
18	0.99	0.02	0.98	0.99	1.03	0.03	1.01	1.05	1.10	0.09	1.01	1.17	0.002	N.S.
19	1.07	0.02	1.07	1.08	1.09	0.04	1.06	1.12	1.18	0.13	1.04	1.26	N.S.	N.S.
21	1.01	0.02	1.00	1.02	1.03	0.02	1.01	1.04	1.10	0.13	0.98	1.18	0.035	0.001
22	1.03	0.02	1.03	1.04	1.04	0.02	1.02	1.06	1.15	0.08	1.10	1.25	N.S.	N.S.
24	1.03	0.02	1.03	1.04	1.05	0.01	1.05	1.06	1.11	0.10	1.03	1.21	0.004	N.S.
26	1.01	0.02	1.01	1.02	1.02	0.01	1.01	1.03	1.07	0.14	0.89	1.15	N.S.	0.027
27	1.01	0.01	1.00	1.01	1.02	0.03	0.99	1.04	1.08	0.06	1.02	1.12	0.037	N.S.
29	1.01	0.02	1.00	1.01	1.02	0.01	1.01	1.03	1.09	0.09	1.02	1.17	N.S.	N.S.
30	1.05	0.02	1.04	1.05	1.05	0.02	1.04	1.07	1.08	0.12	0.92	1.15	N.S.	N.S.
32	1.01	0.01	1.00	1.01	1.02	0.01	1.01	1.02	1.05	0.11	0.95	1.14	N.S.	N.S.

Table 3.6. Mean (±SD), bootstrap bounds and P value for the s(k) function in the three real case groups.

k	$\bar{s}(k)$	*SD*	*Bootstrap bounds*		$\bar{s}(K)$	*SD*	*Bootstrap bounds*		$\bar{s}(K)$	*SD*	*Bootstrap bounds*		*Level of significance*	
Normal photoreceptor mosaic					*NPDR photoreceptor mosaic*				*IRD photoreceptor mosaic*				*Normal/NPDR*	*Normal/IRD*
1	0.23	0.05	0.21	0.24	0.33	0.08	0.28	0.39	0.58	0.28	0.42	0.88	0.003	0.001
5	0.20	0.06	0.18	0.22	0.32	0.05	0.30	0.38	0.51	0.21	0.39	0.73	0.017	0.004
10	0.25	0.06	0.23	0.27	0.34	0.06	0.30	0.39	0.48	0.08	0.42	0.56	N.S.	N.S.
15	0.31	0.07	0.29	0.34	0.47	0.09	0.40	0.53	0.56	0.07	0.51	0.62	0.013	0.014
20	0.42	0.08	0.40	0.45	0.60	0.12	0.51	0.68	0.75	0.08	0.71	0.85	0.002	0.001
25	0.69	0.15	0.65	0.75	0.79	0.13	0.68	0.87	0.91	0.04	0.88	0.95	N.S.	0.006
30	1.12	0.23	1.05	1.21	1.14	0.27	0.97	1.38	1.01	0.14	0.87	1.10	N.S.	N.S.
35	1.36	0.19	1.30	1.43	1.35	0.17	1.19	1.44	1.17	0.25	1.03	1.43	N.S.	N.S.
40	1.25	0.17	1.19	1.31	1.18	0.15	1.07	1.28	1.04	0.10	0.94	1.11	N.S.	0.029
45	1.09	0.16	1.04	1.14	1.10	0.10	1.03	1.16	1.04	0.10	0.94	1.10	N.S.	N.S.
50	0.97	0.08	0.94	1.00	0.93	0.13	0.85	1.04	0.97	0.05	0.91	1.00	N.S.	N.S.
55	0.93	0.10	0.90	0.96	0.93	0.09	0.86	0.99	0.97	0.07	0.93	1.05	N.S.	N.S.
60	0.95	0.06	0.93	0.97	1.01	0.07	0.94	1.05	0.99	0.03	0.97	1.02	N.S.	N.S.
65	0.96	0.08	0.93	0.98	0.98	0.05	0.95	1.03	1.01	0.07	0.96	1.07	N.S.	N.S.
70	0.99	0.09	0.96	1.02	1.07	0.11	0.98	1.14	1.00	0.05	0.97	1.05	N.S.	N.S.
75	1.02	0.08	0.99	1.06	0.96	0.07	0.92	1.02	0.95	0.06	0.90	1.01	N.S.	N.S.
80	0.98	0.08	0.95	1.00	0.99	0.05	0.96	1.04	1.01	0.04	0.99	1.06	N.S.	N.S.
85	1.02	0.07	0.99	1.04	0.98	0.08	0.92	1.03	0.96	0.05	0.91	0.99	N.S.	N.S.
90	1.02	0.09	0.99	1.06	0.96	0.11	0.84	1.02	0.99	0.06	0.95	1.04	N.S.	N.S.
95	1.02	0.05	1.00	1.04	0.97	0.06	0.92	1.01	1.09	0.07	1.04	1.15	0.048	N.S.

Chapter 4

Clustering of spatial functions profiles extracted from normal and diseased AO cone mosaics

4.1 Introduction

Multivariate-multioccasion phenomena can be studied through a set X of IJT values corresponding to J variables, observed on a set of I units, on T different occasions (different times, places, etc.).
The three-way array X is organized according to three modes: units, variables, and occasions. The most widely collected three-way array is given when, together with units and variables, different time occasions are considered, i.e. repeated recurring surveys, longitudinal surveys and so on.
This kind of three-way data, allows to make inferences about the dynamics of change from crosssectional evidence, with increasing of the degrees of freedom and reducing co-linearity among explanatory variables, respect the two-way dataset. The problem to evaluate a dissimilarity between trajectories was first introduced by considering as measure the result of two weighted components combined using subjective weights [70, 71].
Our three-way dataset is not longitudinal, called the X set of IJS, is composed of the spatial second order function values (J variables), observed on the control and inherited retinal disease (IRD) study groups (I units), at different distance r (S). The dissimilarity between spatial curves were defined as a conic combination of the dissimilarities between trends, velocities and accelerations of the pair of function profiles. The coefficients of the linear combination are estimated maximizing its variance. The proposed methodology was applied only for the *r* values in short range scale by excluding the initial inhibition distance. The individual classification was conducted between the control and IRD groups (see Chap. 3), because the NPDR group showed very similar behaviour of the mean spatial statistic functions of control group, so classification between NPDR and control could need bigger sample size.

4.2 Methods

4.2.1 Trend

Let $X_1, X_2, ..., X_k$ be *k* quantitative variables observed on *n* units (subjects) at *r* consecutive space points. The observed data can be arranged into a three-way data set:

$$\mathbf{X} \equiv \left[\mathbf{x}_{i\cdot r} = (x_{i1r}, x_{i2r}, ..., x_{ikr}) : i \in I, r \in S\right] \equiv \left[x_{ijr} : i \in I,\ j \in J, r \in S\right] \quad (4.1)$$

where x_{ijr} is the value of the *j*-th variable (spatial statistic curves) collected on the *i*-th object (subject in our case) at space *r*; $I = \{1,...,n\}$, $J = \{1,...,k\}$, and $S = \{1,...,u\}$ are the set of indices pertaining to objects (subjects in our case), variables and space points, respectively.

The observed objects can be represented as points of a vectorial space equipped with a distance, i.e. a real function δ on the set $\mathbf{Y} \equiv [\mathbf{y}_{i\cdot r} = (x_{i1r}, x_{i2r},..., x_{ikr}, r) : i \in I, r \in S]$ from: $\mathbf{Y} \times \mathbf{Y}$ to $\Re^+$, such that: $\delta_r(i,i) = 0$, $\delta_r(i,l) = \delta_r(l,i)$, $\delta_r(i,l) \geq 0$, $\delta_r(i,l) + \delta_r(h,l) \geq \delta_r(i,h)$, $\forall\, i,\, l,\, h \in I$, where $\delta_r(i,l)$ indicates the distance between subject *i* and *l* of I, at space *r*. Let $M^{k+1} \equiv (\mathbf{Y}, d)$ be the metric space spanning the *k* variables and space.

For each object *i*, $Y(i) \equiv \{\mathbf{y}_{i\cdot r} : r \in S\}$ describes a *space trajectory* of the *i*-th subject according to the *k* examined variables. The trajectory $Y(i)$ is geometrically represented by $u-1$ segments connecting *u* points $\mathbf{y}_{i\cdot r}$ of M^{k+1}.

4.2.2 Velocity and acceleration

Velocity and acceleration are two trajectories' characteristics strongly describing changes of curves along space. In 2-D space, velocity of each segment of the trajectory is the slope of the straight line passing through it: if velocity is negative (positive) the slope will be negative (positive) and the angle made by each segment of the trajectory with the positive direction of the r-axis will be obtuse (acute). Velocity of *Y*(*i*) is defined as the rate of change of *i*-th object position in a fixed space interval and indicating the direction and versus of each segment of the trajectory *Y*(*i*) for a given variable.

Geometrically, acceleration of each pair of segments of trajectory represents their convexity or concavity. If acceleration is positive (negative) the trajectory of the two segments is convex (concave). Acceleration measures the variation of velocity of Y(i) in a fixed space interval.

In this work, the dissimilarity between space trajectories was defined as a linear combination of distances between trends, velocities and accelerations of a pair of trajectories.

Therefore, for each space trajectory *Y*(*i*), the velocity of evolution of an object *i* in the interval from *r* to *r*+1, denoted $s_{r,r+1}$, is, for the *j*-th variable:

$$v_{ijr,r+1} = \frac{x_{ijr+1} - x_{ijr}}{s_{r,r+1}} \qquad (4.2)$$

with $v_{ijr,r+1} > 0$ ($v_{ijt,r+1} < 0$) if object *i*, for the *j*-th variable, presents an increasing (decreasing) rate of change of its position in the space interval from *r* to *r*+1; $v_{ijr,r+1} = 0$ if the object *i* for the *j*-th variable, does not change position from *r* to *r*+1.

For each r of the trajectory Y(i), the acceleration of an object i in the interval from r to r+2, denoted $s_{r,r+2}$, is, for the j-th variable:

$$a_{ijr,\,r+2} = \frac{v_{ijr+1,r+2} - v_{ijr,r+1}}{s_{r,\,r+2}} \qquad (4.3)$$

and $a_{ijr,r+2} > 0$ ($a_{ijr,r+2} < 0$) if the object i, for the j-th variable, presents an increasing (decreasing) variation of velocity in the space interval from r to r+2; $a_{ijr,r+2} = 0$ if object i, for j-th variable, does not change velocity from r to r+2.

4.2.3 Dissimilarity matrix

The dissimilarity between trajectories maybe represented as a function of distances between multivariate objects, $\delta_r(i,l), r \in S$, by the normalized Minkowski metric of order p (in our case we fixed p=2 for Euclidean metric). The distances between trends in a space point *r*, velocities and accelerations in a space interval for object i and l are respectively:

$${}_1\delta_r(i,l) = \frac{1}{\pi_1}\left[\sum_{j=1}^{k}\left|x_{ijr} - x_{ljr}\right|^p\right]^{1/p},\quad {}_2\delta_{r,r+1}(i,l) = \frac{1}{\pi_2}\left[\sum_{j=1}^{k}\left|v_{ijr,r+1} - v_{ljr,r+1}\right|^p\right]^{1/p},\quad {}_3\delta_{r,r+2}(i,l) = \frac{1}{\pi_3}\left[\sum_{j=1}^{k}\left|a_{ijr,r+2} - a_{ljr,r+2}\right|^p\right]^{1/p}$$

(trends distance) (velocities distance) (accelerations distance)

where p is an integer ≥1, and π_1, π_2 and π_3 are suitable weights to normalize distances. Differences between trend intensities, in a space point r, of objects i and l are evaluated according to a measure of distance between $\mathbf{x}_{i.r}$ and $\mathbf{x}_{l.r}$, $r \in S$; differences between velocities of objects i and l, in a space interval, are evaluated according a measure of distance between $\mathbf{v}_{i\cdot r,r+1} = (v_{i1r,r+1},...,v_{ikr,r+1})'$ and $\mathbf{v}_{l\cdot r,r+1}$, r=1,...,u-1; differences between accelerations of objects i and l, in a space interval, are evaluated according to a measure of distance between $a_{i\cdot r,r+2} = (a_{i1r,r+2},...,a_{ikr,r+2})'$ and $a_{l\cdot r,r+2}$, $r = 1,...,u-2$.

A dissimilarity between trends of Y(i) and Y(l) is a mapping from $\{{}_1\delta_r(i,l), r \in S\}$ to $\Re^+$; between velocities of Y(i) and Y(l), a mapping from $\{{}_2\delta_{r,r+1}(i,l), r \in S\}$ to $\Re^+$; and between accelerations of Y(i) and Y(l), a mapping from $\{{}_3\delta_{r,r+2}(i,l), r \in S\}$ to $\Re^+$.

The total dissimilarity between space trajectories *Y*(*i*) and *Y*(*l*) is mapped by the following weighted sum:

$$d^*(i,l) = \sum_{m=1}^{3} \gamma_m d_m(i,l),\ m = 1,2,3 \qquad (4.4)$$

where γ_m, m=1,2,3, are suitable positive weights, that indicate the contribution of each trajectory characteristic to determine the total dissimilarity $d^*(i,l)$.

To follow an objective approach to evaluate weights, we maximized the variance of (4.4), as show below.

Let $\mathbf{D}^* = [d^*(i,l)]$ be the ($n \times n$) matrices of total dissimilarities between trajectories and let $\mathbf{D}_m = [d_m(i,l)]$ be the ($n \times n$) matrices obtained considering the dissimilarities between Y(i) and Y(l) for the three (m=1,2,3) features of each trajectory. Matrices $\mathbf{D}^*$ and $\mathbf{D}_m$ may be represented as vectors defined by elements of a triangle below (above) the diagonal of the matrices $\overline{vec}(\mathbf{D}^*)$ and $\overline{vec}(\mathbf{D}_m)(m = 1,2,3)$. Therefore, $\mathbf{D}_m = \left[\overline{vec}(\mathbf{D}_m)\right] = \left[\overline{vec}(\mathbf{D}_1), \overline{vec}(\mathbf{D}_2), \overline{vec}(\mathbf{D}_3)\right]$ $(m = 1,2,3)$ is a (n(n-1)/2 × 3) matrix; while $\overline{vec}(\mathbf{D}^*) = \sum_{m=1}^{3} \gamma_m \overline{vec}(\mathbf{D}_m)$.

To compute the total dissimilarity between each pair of time trajectories, $\overline{vec}(\mathbf{D}^*)$, the follow problem with respect to variables $\gamma_m = (\gamma_1, \gamma_2, \gamma_3)'$ has to be solved:

$$\begin{cases} max \operatorname{var}(\overline{vec}(\mathbf{D}^*)) = \operatorname{var}(\sum_{m=1}^{3} \gamma_m \overline{vec}(\mathbf{D}_m)) \\ \gamma_m{}'\ \gamma_m = 1 \end{cases} \qquad (4.5)$$

The solution is obtained differentiating the Lagrangian function of (4.5) and equating to zero:

$$\frac{\partial}{\partial \gamma_m}\left[\operatorname{var}(\overline{vec}(\mathbf{D}^*)) + \lambda(1 - \gamma_m{}'\ \gamma_m)\right] = 0, \qquad (4.6)$$

where λ is the Lagrange multiplier. Since $\mathrm{var}(\overline{vec}(\mathbf{D}^*)) = \gamma_m' \sum \gamma_m$, where $\boldsymbol{\Sigma}$ is the variance and covariance matrix of ${}_m\mathbf{D}$; thus equation (4.4) is: $(\sum - \lambda \mathbf{I})\gamma_m = 0$. Then multiplying for γ_m': $\gamma_m' \sum \gamma_m = \lambda$ corresponding to the maximum eigenvalue of $\boldsymbol{\Sigma}$ and γ_m is the associated eigenvector.

4.2.4 Dataset

For every subject belonging to the control (n=33, numbered from 1 to 33) and inherited retinal disease (IRD, n=4, numbered from 34 to 37), we considered the curves of the five spatial statistic functions including G(r), K(r), L(r), $g_2(r)$ and s(k), studied in the chapter 3. Our three-way dataset was composed of the spatial function values for each study subject at a specific interval of distance r. We analysed the curve profiles in the interval distance (Table 4.1) that gave significant differences between control and disease groups in the previous chapter 3.

Table 4.1. Dataset of study

Study groups	**Spatial functions**	**Distance interval (μm)**
N= 33 Healthy subjects (numbered from 1 to 33) N= 4 IRD patients (numbered from 34 to 37)	G(r)	6-18
	K(r)	10-20
	L(r)	7-20
	$g_2(r)$	4-14
	S(k)	1-25

4.3 Results

Clustering analysis was performed using Matlab (version R2013a, The Mathworks Inc., Natick MA, USA). Fixing p=2, in the Minkowski metric the dissimilarity, between trajectories of trend, velocity and acceleration, matrices $\pi_1 D_1$, $\pi_2 D_2$ and $\pi_3 D_3$ were computed. To determine the total dissimilarity matrix, the weights γ_1, γ_2, γ_3 were computed as described in paragraph 4.2.3, by finding the largest

eigenvalue and the associated eigenvector of Σ. The values of λ and $\gamma = (\gamma_1, \gamma_2, \gamma_3)$ for each spatial statistic function are shown in Table 4.2.

Table 4.2. Values of the largest eigenvalue and the associated eigenvector for the spatial functions.

	G(r)	**K(r)**	**L(r)**	**g_2(r)**	**S(k)**
λ	2.5106	2.4111	2.2421	2.2226	2.4356
γ_1	0.3129	0.3561	0.2795	0.2457	0.2890
γ_2	0.3595	0.3563	0.3724	0.3782	0.3636
γ_3	0.3276	0.2876	0.3481	0.3761	0.3474

Finally, the method of Ward (minimum variance algorithm) linkage was applied to the matrix $\mathbf{D}^*$. The dendrograms relative to the dissimilarity matrices of the five studied spatial functions are shown in Figures 4.1-5. The vertical axis of the dendrogram represents the distance or dissimilarity between clusters. The horizontal axis represents the subjects and clusters.

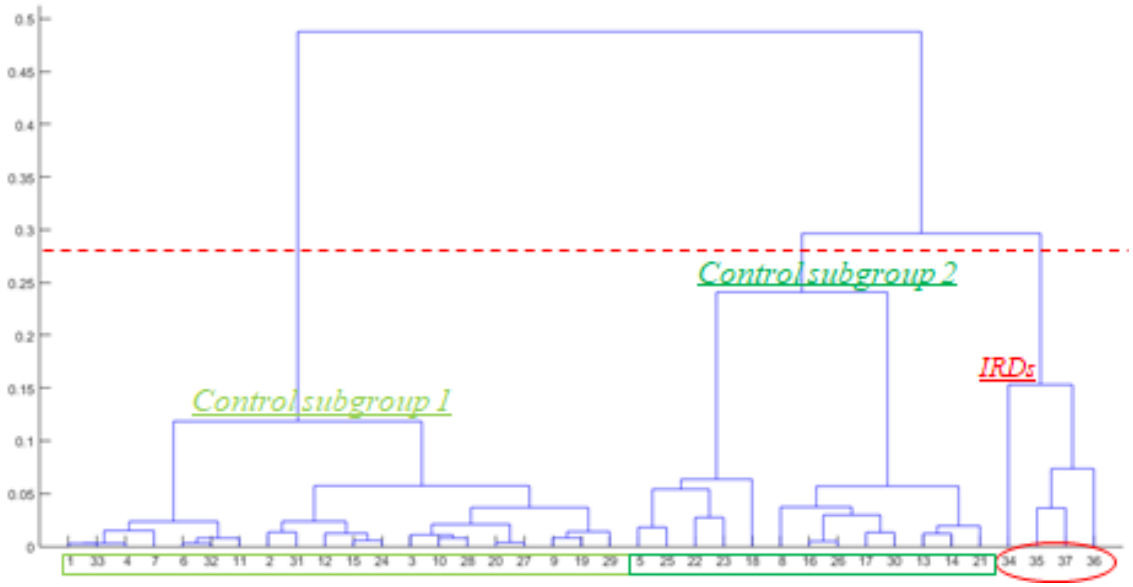

Figure 4.1. Dendrogram of the G(r) function in all subjects. Looking at this dendrogram, under the red pruning line we can see three clusters, 2 of the control group and 1 with the IRD patients (34-37). The individual profiles of the control group appeared to be not enough homogenous to constitute one cluster.

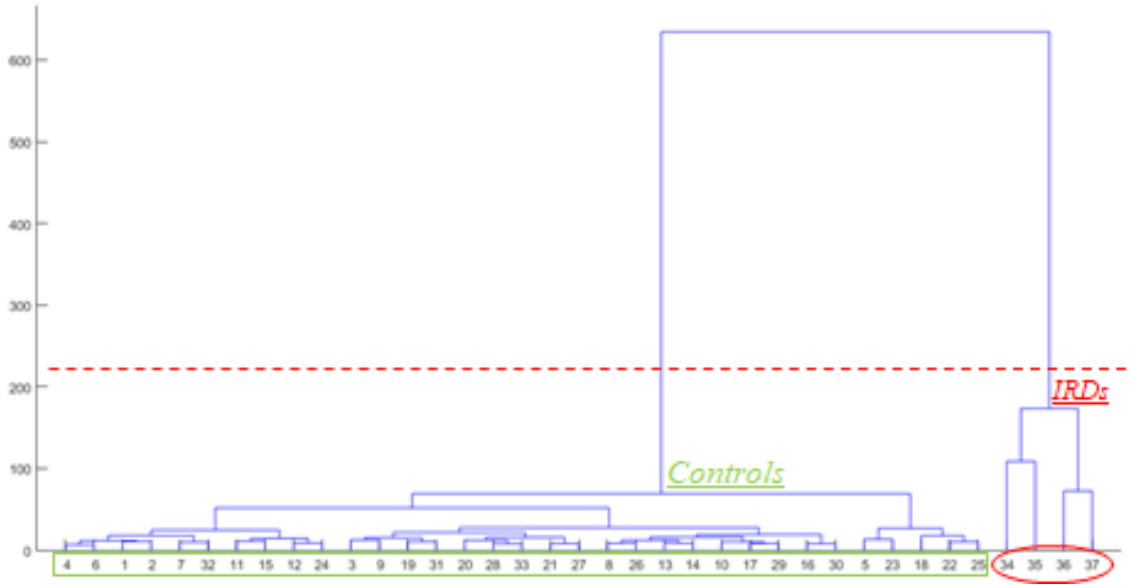

Figure 4.2. Dendrogram of the individual trajectories of the K(r) function, in red pruning line. In this graph, the pruning line divided the study in group in two clusters: the first composed of all the healthy subjects, and the second of only the IRD patients. The K(r) function allowed as to differentiate exactly between o

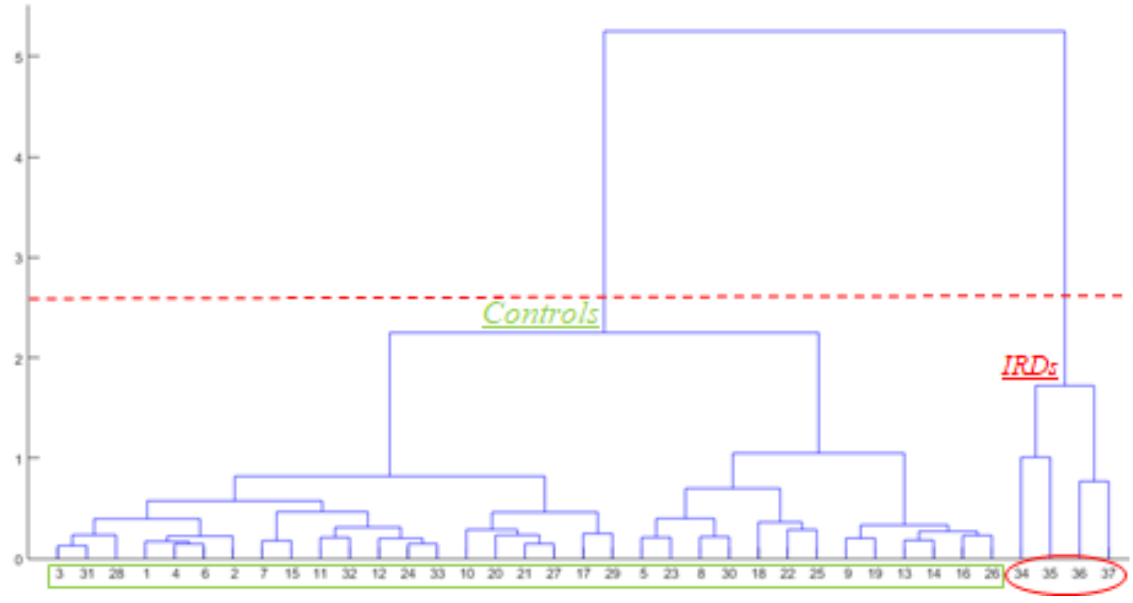

Figure 4.3. Dendrogram of the r trajectories of the L(r) function in all the subjects, in red pruning line. The L(r) function information derive from the K(r) function, so also in this dendrogram we identified exactly our two study groups.

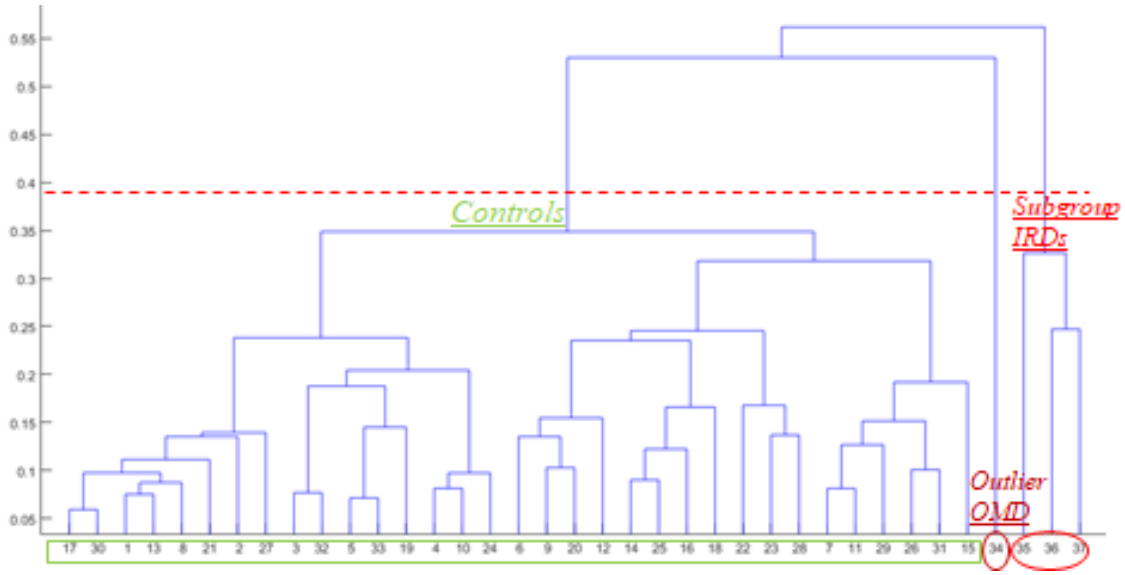

Figure 4.4. Dendrogram of individual trajectories of the $g_2(r)$ function. The red pruning line divides the subject in three groups: one composed of all the healthy subjects, the other with three subjects of the IRD group and the third composed of the outlier 34.

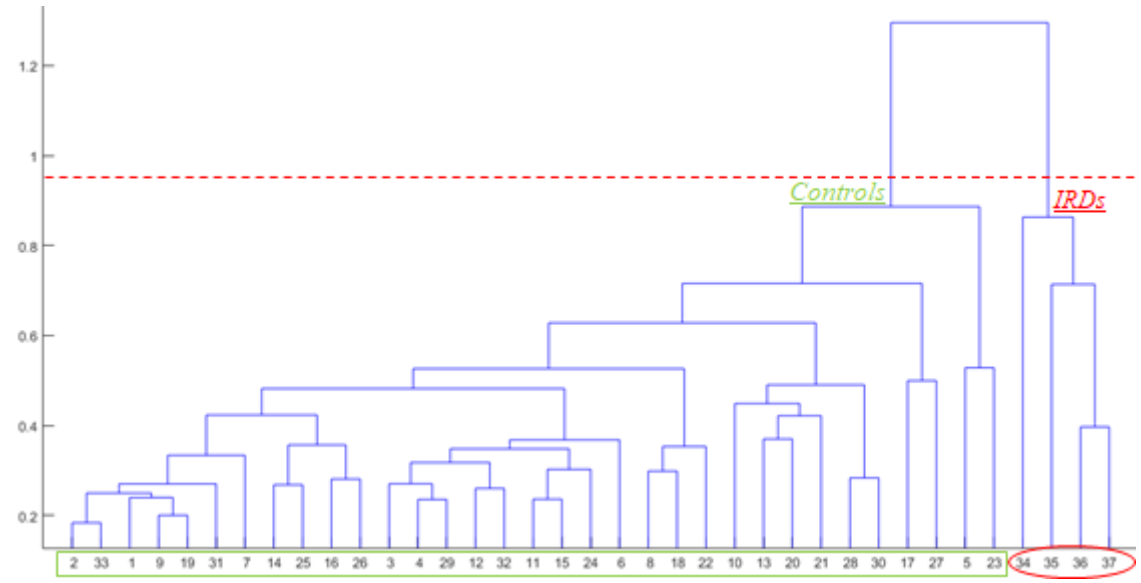

Figure 4.5. Dendrogram of the r trajectories of the s(k) function in all the subjects, in red pruning line. In this dendrogram we identified under the pruning line two clusters composed exactly of members of the two study groups IRD and control.

4.4 Discussion

In this chapter, a method to analyse dissimilarities between spatial function profiles have been discussed. In this case with application to a dataset where the function curves varied with distance *r*, instead of time *t*.

The used model was a combination of distances between trends, velocities and accelerations measured on the spatial second order function, seen in the chapter 4. Aim of this analysis was to try a clustering analysis of spatial functions extracted in the AO mosaic images in the control and IRD groups.

The results showed that the right classification of the subjects in the two study groups was performed with the K(r), L(r) and s(k) functions, while with the G(r) and the pair correlation function $g_2(r)$ the control and the IRD groups appeared to be not enough homogenous.

This is a first attempt to apply such type of analysis based on dynamic curves study, to spatial functions extracted from biomedical images.

Conclusion

This thesis has shown different techniques to quantify the information of the cone arrangement in the retinal mosaic.

The first approach is a classical global way to extract spacing descriptors of the distribution cones, that gives helpful information summarizing the distance between neighbour cones. We evaluated the agreement between three metrics (S_{cc}, LCS and DRPD) currently used to describe the distribution of distances between cones in AO images of the cone mosaic in a group of healthy subjects and a group of patients with different retinal diseases and variable loss of cone reflectivity. The aim was to understand if the three considered metrics, which have been calculated over sampling areas of different size, could be used interchangeably in clinical studies. It emerged that the influence of the sampling window size is important and the choice of the window size should avoid poor sampling. The use of smaller sampling windows allows for a local analysis of the integrity of the cone mosaic, while the use of larger areas may lead to overestimating the integrity of the retinal mosaic. Care is needed when comparing results of these kind of metrics in different clinical study.

In the second approach, classical inference methods and bootstrap techniques were applied to compare mean second order functions of three groups of cases. For this purpose, a pointwise, local approach with consecutive significance tests at all r/k-values, was chosen. This method overcomes issue relative to the selection of the window sampling size and gives information about the arrangement of the cones mosaic ad short and long range. The comparison between the three study groups was done by a descriptive analysis of the mean spatial functions at specific r values.

Finally, starting from these results, a first attempt of individual curves classification was made in order to cluster the subjects in homogeneous classes corresponding to the normal or pathological state.

The good results obtained with the statistical point pattern analysis suggest as next step, to improve this analysis by fitting a model to the cone mosaic in normal and diseased subjects.

Bibliography

[1] Lombardo, M., Serrao, S., Devaney, N., Parravano, M., & Lombardo, G. (2013). Adaptive optics technology for high-resolution retinal imaging. Sensors, 13(1), 334-366.

[2] Hildebrand, G. D., & Fielder, A. R. (2011). Anatomy and physiology of the retina. In Pediatric retina (pp. 39-65). Springer Berlin Heidelberg.

[3] Méry, J. (1704). Des mouvements de l'Iris et par occasion de la partie principale de l'organe de la Vuë. Mémoire de l'Açademie des Sciences, 23, 277-284.

[4] Helmholtz, H. (1851). Beschreibung des Augenspiegels (pp. 28-34): Springer Berlin Heidelberg.

[5] Hageman, G. S., Gehrs, K., Johnson, L. V., & Anderson, D. (1995). Webvision: the organization of the retina and visual system. Salt Lake City, UT: University of Utah Health Sciences Center.

[6] Schnapf, J. L. and D. A. Baylor (1987) How photoreceptor cells respond to light. Sci. Am. 256 (April): 40–47.

[7] Tachibanaki, S., Arinobu, D., Shimauchi-Matsukawa, Y., Tsushima, S., & Kawamura, S. (2005). Highly effective phosphorylation by G protein-coupled receptor kinase 7 of light-activated visual pigment in cones. Proceedings of the National Academy of Sciences of the USA, 102(26), 9329-9334.

[8] Tachibanaki, S., Tsushima, S., & Kawamura, S. (2001). Low amplification and fast visual pigment phosphorylation as mechanisms characterizing cone photoresponses. Proceedings of the National Academy of Sciences of the USA, 98(24), 14044-14049.

[9] Weiss, E. R., Ducceschi, M. H., Horner, T. J., Li, A., Craft, C. M., & Osawa, S. (2001). Species-specific differences in expression of G-protein-coupled receptor kinase (GRK) 7 and GRK1 in mammalian cone photoreceptor cells: implications for cone cell phototransduction. Journal of Neuroscience, 21(23), 9175-9184.

[10] Neuroscience. 2nd edition. Purves D, Augustine GJ, Fitzpatrick D, et al., editors. Sunderland (MA): Sinauer Associates; 2001.

[11] Charman, W.N.; Chateau, N. The prospects for super-acuity: Limits to visual performance after correction of monochromatic ocular aberration. Ophthalmic Physl. Opt. 2003, 23, 479–493.

[12] Williams, D.R.; Yoon, G.Y.; Porter, J.; Guirao, A.; Hofer, H.; Cox, I. Visual benefit of correcting higher order aberrations of the eye. J. Refract. Surg. 2000, 16, S554–S559.

[13] Williams, D.R. Imaging single cells in the living retina. Vis. Res. 2011, 51, 1379–1396.

[14] Godara, P.; Dubis, A.M.; Roorda, A.; Duncan, J.L.; Carroll, J. Adaptive optics retinal imaging: Emerging clinical applications. Optom. Vis. Sci. 2010, 87, 930–941.

[15] Dreher, A.W.; Bille, J.F.; Weinreb, R.N. Active optical depth resolution improvement of the laser tomographic scanner. Appl. Opt. 1989, 28, 804–808.

[16] Liang, J.; Miller, D.T.; Williams, D.R. Supernormal and high-resolution retinal imaging through adaptive optics. JOSA A 1997, 14, 2884–2892.

[17] M. Zacharria, B. Lamory, and N. Chateau, "Biomedical imaging: New view of the eye," Nature Photonics, vol. 5, pp. 24–26, Jan. 2011.

[18] C. Viard, K. Nakashima, B. Lamory, M. Paques, X. Levecq, and N. Chateau, "Imaging microscopic structures in pathological retinas using a floodillumination adaptive optics retinal camera," in Opthalmic Technologies XXI, vol. 12, pp. 7885091–78850910, 2011.

[19] Curcio, C. A., Sloan, K. R., Kalina, R. E., & Hendrickson, A. E. (1990). Human photoreceptor topography. Journal of Comparative Neurology, 292(4), 497-523.

[20] Pum, D., Ahnelt, P. K., & Grasl, M. (1990). Iso-orientation areas in the foveal cone mosaic. Visual Neuroscience, 5, 511-523.

[21] Kolb, H., Fernandez, E., & Nelson, R. (2011). Webvision: Simple anatomy of the retina.

[22] Cooper, Robert Francis, "Noninvasive Assessment of Photoreceptor Structure and Function in the Human Retina" (2015). Dissertations (2009 -). Paper 590.

[23] Carroll J, Kay D, Scoles D, Dubra A, Lombardo M. Adaptive optics retinal imaging – Clinical opportunities and challenges. Curr Eye Research 2013; 38(7): 709-721.

[24] Roorda A, Duncan JL. Adaptive optics ophthalmoscopy. Annu Rev Vis Sci 2015;1:19-50.

[25] Duncan JL, Zhang Y, Gandhi J, Nakanishi C, Othman M, Branham KE, Swaroop A, Roorda A. High-resolution imaging with adaptive optics in patients with inherited retinal degeneration. Invest Ophthalmol Vis Sci 2007; 48(7):3283-3291.

[26] Garrioch R, Langlo C, Dubis AM, Cooper RF, Dubra A, Carroll J. Repeatability on in vivo cone density and spacing measurements. Optom Vis Sci 2012; 89, 632-643.

[27] Lombardo M, Lombardo G, Schiano Lomoriello D, Ducoli P, Stirpe M, Serrao S. Interocular symmetry of parafoveal photoreceptor cone density distribution. Retina 2013; 33(8): 1640-1649.

[28] Talcott KE, Ratnam K, Sundquist SM, Lucero AS, Lujan BJ, Tao W, Porco TC, Roorda A, Duncan JL. Longitudinal study of cone photoreceptors during retinal degeneration and in response to ciliary neurotrophic factor treatment. Invest Ophthalmol Vis Sci 2011;52:2219-2226.

[29] Zhang T, Godara P, Blanco ER, Griffin RL, Wang X, Curcio CA, Zhang Y. Variability in human cone topography assessed by adaptive optics scanning laser ophthalmoscopy. Am J Ophthalmol 2015;160(2):290-300.

[30] Lombardo M, Serrao S, Ducoli P, Lombardo G. Influence of sampling window size and orientation on parafoveal cone packing density. Biomed Opt Express 2013; 4(8):1318-1331.

[31] Lombardo M, Serrao S, Lombardo G. Technical factors influencing cone packing density estimates in adaptive optics flood illuminated retinal images. PloS One 2014; 9(9): e107402.

[32] Chiu S J, Lokhnygina Y, Dubis AM, Dubra A, Carroll J et al. Automatic cone photoreceptor segmentation using graph theory and dynamic programming. Biomed Opt Express 2013; 4(6): 924-937.

[33] Mariotti L, Devaney N, Lombardo G, Lombardo M. Understanding the changes of cone reflectance in adaptive optics flood illumination retinal images over 3 years. Biomed Opt Expr 2016; 7: 2807-2822.

[34] Cooper RF, Wilk MA, Tarima S, Carroll J. Evaluating descriptive metrics of the human cone mosaic. Invest Ophthalmol Vis Sci 2016; 57: 2992-3001.

[35] Zayit-Soudry S, Sippl-Swezey N, Porco TC, Lynch SK, Syed R, Ratnam K, Menghini M, Roorda AJ, Duncan JL. Repeatability of cone spacing measures in eyes with inherited retinal degenerations. Invest Ophthalmol Vis Sci 2015; 56(10): 6179-6189.

[36] Chui TY, Song H, Burns SA. Individual variations in human cone photoreceptor packing density: variations with refractive error. Invest Ophthalmol Vis Sci 2008; 49(10): 4679-4687.

[37] Li KY, Tiruveedhula P, Roorda A. Intersubject variability of foveal cone photoreceptor density in relation to eye length. Invest Ophthalmol Vis Sci 2010; 51(12): 6858-6867.

[38] Hirsch J, Miller WH. Does cone positional disorder limit resolution? J Opt Soc Am A 1987; 4(8): 1481-1489.

[39] Rodieck RW. The density recovery profile: a method for the analysis of points in the plane applicable to retinal studies. Vis Neurosci 1991; 6: 95-111.

[40] Galli-Resta L, Novelli E, Kryger Z, Jacobs GH, Reese BE. Modelling the mosaic organization of rod and cone photoreceptors with a minimal-spacing rule. Eur J Neurosci 1999; 11: 1461-1469.

[41] Ferris FL 3rd, Wilkinson CP, Bird A, Chakravarthy U, Chew E, Csaky K, Sadda SR. Clinical classification of age-related macular degeneration. Ophthalmology 2013; 120: 844-851.

[42] Khan KN, Mahroo OA, Khan RS, Mohamed MD, McKibbin M, Bird A, Michaelides M, Tufail A, Moore AT. Differentiating drusen: Drusen and drusen-like appearances associated with ageing, age-related macular degeneration, inherited eye disease and other pathological processes. Prog Retin Eye Res 2016; 53: 70-106.

[43] Early Treatment Diabetic Retinopathy Study Research Group (1991) Grading diabetic retinopathy from stereoscopic color fundus photographs: an extension of the modified Airlie House classification. ETDRS report number 10. Ophthalmology 98 (suppl): 823-833.

[44] Lombardo M, Parravano M, Serrao S, Ziccardi L, Giannini D, Lombardo G. Investigation of adaptive optics imaging biomarkers for detecting pathological changes of the cone mosaic in patients with type 1 diabetes mellitus. PLoS One 2016; 11: e0151380.

[45] Ziccardi L, Giannini D, Lombardo G, Serrao S, Dell'Omo R, Nicoletti A, Bertelli M, Lombardo M. Multimodal approach to monitoring and investigating cone structure and function in an inherited macular dystrophy. Am J Ophthalmol 2015; 160(2): 301-312.

[46] Drasdo N, Fowler CW. Non-linear projection of the retinal image in a wide-angle schematic eye. Br J Ophthalmol 1974;58:709-714.

[47] Coletta NJ, Watson T. Effect of myopia on visual acuity measured with laser interference fringes. Vis Res 2006; 46: 636-651.

[48] Li KY, Roorda A. Automated identification of cone photoreceptors in adaptive optics retinal images. J Opt Soc Am A 2007; 24: 1358-1363.

[49] Lombardo M, Serrao S, Ducoli P, Lombardo G. Eccentricity dependent changes of density, spacing and packing arrangement of parafoveal cones. Ophthalmic Physiol Optics 2013;33: 516-526.

[50] Brostow W, Dussault JP, Fox BL. Construction of Voronoi polyhedra. J Comput Physics 1978; 29: 81-92.

[51] Lammer J, Prager SG, Cheney MC, Ahmed A, Radwan SH, Burns SA,Silva PS, Sun JK. Cone photoreceptor irregularity on adaptive optics scanning laser ophthalmoscopy correlates with severity of diabetic retinopathy and macular edema. Invest Ophthalmol Vis Sci 2016; 57: 6624-6632.

[52] Yellott Jr JI. Spectral analysis of spatial sampling by photoreceptors: topological disorder prevents aliasing. Vision Res 1982; 22: 1205-1210.

[53] Lombardo M, Serrao S, Ducoli P, Lombardo G. Variations in the image optical quality of the eye and the sampling limit of resolution of the cone mosaic with axial length in young adults. J Cataract Refract Surg 2012; 38: 1147-1155.

[54] Muthiah MN, Gias C, Chen FK, Zhong J, McClelland Z, Sallo FB, Peto T, Coffey PJ, da Cruz L. Cone photoreceptor definition on adaptive optics retinal imaging. Br J Ophthalmol 2014; 98: 1073-1079.

[55] Cooper RF, Lombardo M, Carroll J, Sloan KR, Lombardo G. Methods for investigating the local spatial anisotropy and the preferred orientation of cones in adaptive optics retinal images. Vis Neurosci 2016; 33: E005.

[56] Curcio CA, Sloan KR. Packing geometry of human cone photoreceptors: variation with eccentricity and evidence of local anisotropy. Vis Neuroscience 1992; 9: 169-180.

[57] Shapiro MB, Schein SJ, De Monasterio FM. Regularity and Structure of the Spatial Pattern of Blue Cones of Macaque Retina. J Am Stat Assoc 1985; 80(392): 803-812.

[58] Duyckaerts C, Godefroy G. Voronoi tessellation to study the numerical density and the spatial distribution of neurones. J Chem Neuroanat 2000; 20: 83-92.

[59] Cook JE. Spatial properties of retinal mosaics: an empirical evaluation of some existing measures. Vis Neurosci 1996; 13: 15-30.

[60] Putnam NM, Hofer HJ, Doble N, Chen L, Carroll J, Williams DR. The locus of fixation and the foveal cone mosaic. J Vision 2005; 5: 632-639.

[61] Scoles D, Sulai YN, Langlo CS, Fishman GA, Curcio CA, Carroll J, Dubra A. In Vivo imaging of human cone photoreceptor inner segments. In vivo imaging of photoreceptor inner segments. Invest Ophthalmol Vis Sci 2014;55(7):4244-4251.

[62] Jiao, Y., Berman, H., Kiehl, T. R., & Torquato, S. (2011). Spatial organization and correlations of cell nuclei in brain tumors. PloS one, 6(11), e27323.

[63] Mattfeldt, T., Eckel, S., Fleischer, F., & Schmidt, V. (2006). Statistical analysis of reduced pair correlation functions of capillaries in the prostate gland. Journal of Microscopy, 223(2), 107-119.
[64] Torquato S (2011) Toward an Ising model of cancer and beyond. Physical Biology 8: 015017.

[65] Torquato S (2002) Random Heterogeneous Materials: Microstructure and Macroscopic Properties: Springer-Verlag. 701 p.

[66] Cressie, N. (1991). Spatial statistics. New York: John “filey.

[67] Diggle, P. J. (1983). Statistical analysis of spatial point processes. Academic, London.

[68] Ripley, B.D. (1988) Statistical Inference for Spatial Processes. Cambridge:

Cambridge University Press.

[69] Stoyan, D. & Stoyan, H. (1994) Fractals, Random Shapes and Point

Fields. Methods of Geometrical Statistics. Chichester: Wiley.

[70] D’Urso, Pierpaolo, and Maurizio Vichi. "Dissimilarities between trajectories of a three-way longitudinal data set." *Advances in data science and classification*. Springer Berlin Heidelberg, 1998. 585-592.

[71] Carlier, A. (1986). Factor Analysis of Evolution and Cluster Methods on Trajectories, Proceedings of COMPSTAT’86, Physica-Verlag, Heidelberg Wien, 140-145.